Synthesis, Antimicrobial, DFT, and In Silico Pharmacokinetic Profiling of Nitroaldol Quinoline Derivatives: A Comprehensive Exploration for Designing Potential Oral Antibacterial Agents Targeting DNA-Gyrase

Fatiha Guenfoud, Oussama Khaoua, Zineb Cherak, Lotfi Loucif, Walid Boussebaa, Noura Benbellat, Mouhammed Laabassi, Paul Mosset

Highlights

- The Henry reaction was employed to synthesize nine novel β-nitroaldol quinoline derivatives.
- The chemical structures were confirmed by several spectroscopic techniques.
- The antibacterial and antifungal activities were assessed using the *in vitro* method.
- The chemical reactivity and ligand-DNA gyrase interactions were investigated by DFT and Molecular Docking studies.
- The gastrointestinal absorption and the inhibitory effects on specific enzymes were identified through several pharmacokinetic parameters.

Synthesis, Antimicrobial, DFT, and *In Silico* Pharmacokinetic Profiling of Nitroaldol Quinoline Derivatives: A Comprehensive Exploration for Designing Potential Oral Antibacterial Agents Targeting DNA-Gyrase

Fatiha Guenfoud*[a,b], Oussama Khaoua[a], Zineb Cherak[c], Lotfi Loucif[d], Walid Boussebaa[e], Noura Benbellat*[a], Mouhammed Laabassi[f], Paul Mosset[j].

[a]*Laboratoire de Chimie des Matériaux et des Vivants: Activité & Réactivité (LCMVAR), Département de Chimie, Faculté des Sciences de la Matière, Université de Batna-1, Algérie.*

[b]*Département de Pharmacie, Faculté de Sciences Médical, Université de Batna 2, Algérie.*

[c]*Faculté des Sciences de la Nature et de la Vie, Université de Batna 2, Algérie.*

[d]*Laboratoire de Biotechnologie des Molécules Bioactives et de la Physiopathologie Cellulaire (LBMBPC), Faculté des Sciences de la Nature et de la Vie, Université de Batna 2, Algérie.*

[e]*Laboratoire de Génétique, Biotechnologie et Valorisation des Bio-ressources (GBVB), Faculté des Sciences Exactes et des Sciences de la Nature et de la Vie, Université Mohamed Khider, Biskra, Algérie.*

[f]*Département des Sciences et Technologies, Faculté de Technologie, Mostafa Benboulaïd, Université de Batna 2, Algérie.*

[j]*CNRS, ISCR (Institut des Sciences Chimiques de Rennes), Université de Rennes, UMR 6226, F-35000 Rennes, France.*

Corresponding authors: Fatiha Guenfoud Tel: +213 667949537; Fax: +213 33319015; E-mail addresses:

* f.guenfoud@univ-batna2.dz;

*noura.benbellat@univ-batna.dz

Abstract

This study presents a thorough exploration of the synthesis, biological activities, and molecular properties of a novel series of nitroaldol quinoline derivatives (**4a**-**4i**). Structural characterization utilized FTIR, mass spectrometry, ^{1}H NMR, and ^{13}C NMR, providing a comprehensive understanding of the synthesized derivatives. Moreover, anti-microbial properties were evaluated using agar disk diffusion assay against five pathogenic strains, including Gram-negative and Gram-positive bacteria, as well as a fungal strain. Notably, compound **4e** demonstrated strong anti-fungal and anti-bacterial activities (MIC = 25 µg/ml). A detailed analysis of molecular orbitals, total density of state, vibrational characteristics, global reactivity descriptors, molecular electrostatic potential, topological QTAIM analysis, and molecular docking provided nuanced insights into the reactivity, electronic properties, and potential interactions of the synthesized compounds. These findings contribute valuable information to the design and synthesis of compounds targeting bacterial DNA-gyrase. Furthermore, *in silico* predictions using the SwissADME online server indicated that all compounds comply with Lipinski's rule of five, suggesting their potential as orally active drugs. The compounds demonstrated commendable water solubility, passed various filters, and exhibited bioavailability scores, indicating promising oral bioavailability. The percentage of oral absorption ranged from 75.39% to 78.58%, signifying high permeability. Computational analysis of pharmacokinetic parameters revealed favorable characteristics, including gastrointestinal absorption and minimal inhibitory effects on specific enzymes.

Keywords: Henry reaction, Nitroaldol quinoline derivatives, Antimicrobial activity, DFT, DNA gyrase, *In silico* SwissADME.

1. Introduction

Antibiotics have facilitated significant therapeutic advances since their discovery in the early 20th century, playing a crucial role in the evolution of modern medicine. Unfortunately, in recent years, bacteria

have become increasingly resistant [1]. This resistance is attributed to the immoderate and often inappropriate prescription of antibiotics [2,3]. The urgency to discover novel antibacterial agents has become paramount. For many years, organic and medicinal chemists have been intrigued by the synthesis of quinoline and its derivatives [4] which demonstrated a wide range of activities [5,6], with several being clinically used as antibacterial [7,8], anti-fungal [9], anti-inflammatory [10], anti-hypertensive [11], anti-malarial [12,13], anti-oxidant [14], anti-cancer [15,16], anti-tubercular [17], analgesic [18], anti-Alzheimer [19], antiviral agents [20].

Ciprofloxacin, a broad-spectrum antibiotic from the fluoroquinolone class, primarily targets bacterial DNA gyrase and topoisomerase IV, essential enzymes involved in bacterial DNA replication and repair [21,22]. By inhibiting the activity of these enzymes, Ciprofloxacin induces the breakdown of bacterial DNA, leading to bacterial cell death. These enzymes are the primary and well-established targets of Ciprofloxacin in bacterial cells. It is commonly used to treat various bacterial infections, including urinary tract infections, respiratory infections, skin infections, and gastrointestinal infections. To assess the interaction between the synthesized molecules and the experimentally selected bacterial strains, a molecular docking study was conducted on the active cavity of DNA gyrase (PDB code: 1KZN).

The Henry reaction, also known as the nitroaldol reaction, holds significant importance and is a valuable process in synthetic organic chemistry. This reaction is commonly employed for the formation of C-C bonds, achieved by combining a carbonyl compound, typically an aldehyde, with either a primary or secondary nitroalkane [23–25]. The β-nitro alcohol derivatives are frequently used as essential intermediates in the synthesis of bioactive molecules such as (R)-isoproterenol, a potent β-adrenoreceptor [26], the α1-adrenergic receptor agonist (R)-phenylephrine [27], core fragments of ritonavir and lopinavir; HIV protease inhibitors [28], and epiquinamide [29].

The objective of this paper is to undertake the synthesis, characterization, spectroscopic analyses (FT-IR, ^{1}H NMR, ^{13}C NMR), mass spectrometry techniques, DFT calculations, *in-silico* studies, and

exploration of the biological activities were performed on a new series of nitroaldol quinoline derivatives (**4a**-**4i**) obtained through the Henry reaction.

The application of computational practices assisted in predicting, exploring, and explaining some chemical properties of molecules, primarily using the DFT approach. Thus, various chemical and electronic properties were investigated and evaluated, such as Molecular Electrostatic Potential (MEP) and Frontier energy gap. Moreover, these molecules were experimentally tested against five strains that are the most frequently used for the screening of antimicrobial activities [30–33] ; two Gram-negative bacteria (*Pseudomonas aeruginosa* ATTC 1117 and *Escherichia coli* ATCC 25922), two Gram-positive bacteria (*Staphylococcus aureus* ATCC 25923, and a clinical vancomycin-resistant *Enterococcus faecium* strain), and a fungal strain (*Candida albicans* ATCC 90029). The *Enterococcus faecium* strain has been selected as a Gram-positive bacterium, serving as a last-resort antibiotic. Finally, the *in-silico* tools were employed to assess oral absorption, membrane permeability efficacy, and drug availability of the synthesized compounds.

2. Materials and methods

2.1. Chemistry

The study utilized various analytical techniques to characterize the compounds. Reaction durations were assessed using TLC on Silica gel plates 60 F254 from E. Merck, with spot visualization under UV light at wavelengths of 254 and 366 nm. Melting point ranges were determined using the Banc Koffler apparatus without correction. ^{1}H NMR and ^{13}C NMR spectra were recorded on a BRUKER AVANCE III HD spectrometer operating at 400 MHz (^{1}H) and 101 MHz (^{13}C). FTIR-ATR spectra were measured in the range 400 – 4000 cm^{-1} using a BRUKER Alpha spectrophotometer at the Scientific and Technical Research Centre in Physico-Chemical Analyses (CRAPC), Bou-Ismail, Tipaza, Algeria. Additional ^{1}H NMR and ^{13}C NMR (HMBC and HMQC) spectra were obtained on a Bruker ARX 400 (400 MHz for ^{1}H, 100 MHz for ^{13}C) at the Centre Regional de Mesures Physiques, Université de Rennes, France, using $CDCl_3$ as a solvent,

tetramethyl silane as an internal reference, and coupling constants (*J* values) in Hertz. Mass spectra were generated on a SHIMADZU GCMS 2010-DI-2010 spectrometer operating at 70 eV at the Scientific and Technical Research Centre in Physico-Chemical Analyses (CRAPC), Ouargla, Algeria.

2.1.1. *Synthesis of 1-(6-Methyl-2-propoxy-quinolin-3-yl)-2-nitro-ethanol* (3d)

In a 100 mL round-bottom flask equipped with a magnetic stirrer, (1.0 g, 5.2 mmol) of 6-Methyl-2-propoxy-3-formyl quinoline (**2d**) (Scheme 1) was dissolved in 30 mL of propanol/DMF (1/1), and (1.5 g, 10.8 mmol) of potassium carbonate was added. The progress of the refluxed reaction was monitored by TLC. After 8 hours, excess propanol was removed by distillation, and 100 mL of ice-cold water was added to the residue once cooled to room temperature. The resulting precipitate of 1-(6-Methyl-2-propoxy-quinolin-3-yl)-2-nitro-ethanol (**3d**) was collected by filtration and washed twice with 20 mL of ice-cold water.

Compound **3d** was obtained as a pistachio green crystals, yield = 90%, R_f = 0.37 (ethyl acetate/petroleum ether: 1/9), M.p = 84-86°C. ^{1}H NMR (400 MHz, $CDCl_3$) δ (ppm) : 10.49 (s, 1H, CHO); 8.48 (s large, 1H, H_4), 7.72 (d, *J* = 8.5 Hz, 1H, H_8), 7.60-7.56 (m, 1H, H_5), 7.54 (ddd large, *J* = 8.5, 2.1, 0.5 Hz, 1H, H_7), 4.52 (t, *J* = 6.6 Hz, 2H, $OC\underline{H}_2$-CH_2-CH_3), 2.48 (s, 3H, C_6-$C\underline{H}_3$), 1.91 (qt, *J* = 7.4, 6.6 Hz, 2H, OCH_2-$C\underline{H}_2$-CH_3), 1.09 (t, *J* = 7.4 Hz, 3H, OCH_2-CH_2-$C\underline{H}_3$). ^{13}C NMR (100 MHz, $CDCl_3$) δ (ppm): 189.63 (CHO), 160.88 (C_2), 147.51 (C_{8a}), 138.96 (C_4), 134.68 (C_7), 134.59 (C_6), 128.62 (C_5), 126.93 (C_8), 124.25 (C_{4a}), 119.94 (C_3), 67.96 ($O\underline{C}H_2$-CH_2-CH_3), 22.27 (OCH_2-$\underline{C}H_2$-CH_3), 21.2 (C_6-CH_3), 10.69 (OCH_2-CH_2-$\underline{C}H_3$).

2.1.2. *General Procedure for the Henry reaction* (4a-4i)

In a 100 mL round-bottom flask, nitromethane (0.3 mL, 5.62 mmol, 10.5 eq.) and the appropriate 2-methoxyquinoline-3-carbaldehyde (100 mg, 0.53 mmol, 1 eq.) were dissolved in 16 mL of EtOH/MeOH (1/1). After introducing a solution of NaOH (0.3 mL, 0.2 M) and cooling the mixture to 0°C using an ice and salt bath, the reaction's progress was monitored by TLC. After 2 hours, 30 mL of water was added to

the mixture, resulting in the formation of a precipitate. This precipitate was subsequently filtered, washed with water, and subjected to purification through silica gel column chromatography, using petroleum ether/ethyl acetate as the eluent."

a) 1-(2-Methoxy-quinolin-3-yl)-2-nitro-ethanol **(4a):**

White crystals, yield = 75%, R_f = 0.3 (ethyl acetate/petroleum ether: 1/9), M.p = 112-114 °C. IR (ATR) ν cm^{-1}: 3200 (OH), 2949 (aliphatic CH), 1627 (aromatic C=C), 1548 (NO_2), 1256 (C-O). ^{1}H NMR (400 MHz, $CDCl_3$) δ (ppm): 8.18 (s, 1H, H_4), 7.85 (d, *J* = 8.4 Hz, 1H, H_8), 7.74 (dd, *J* = 8.1, 1.0 Hz, 1H, H_5), 7.64 (ddd, *J* = 8.4, 7.0, 1.4 Hz, 1H, H_7), 7.41 (ddd, *J* = 8.0, 7.2, 1.2 Hz, 1H, H_6), 5.66 (ddd, *J* = 8.4, 5.2, 2.8 Hz, 1H, C<u>H</u>OH), 4.79 (dd, *J* = 13.4, 2.8 Hz, 1H, H_a, $NO_2C\underline{H}_2$), 4.55 (dd, *J* = 13.4, 9.1 Hz, 1H, H_b, $NO_2C\underline{H}_2$), 4.13 (s,3H, C_2-$OC\underline{H}_3$), 3.31 (d, *J* = 5.6 Hz, 1H, OH). ^{13}C NMR (101 MHz, $CDCl_3$) δ (ppm): 158.48 (C_2), 146.16 (C_{8a}), 136.2 (C_4), 130.08 (C_7), 127.73 (C_5), 127.02 (C_8), 125.02 (C_{4a}), 124.72 (C_6), 121.87 (C_3), 79.45 ($\underline{C}H_2NO_2$), 67.01 (HO-$\underline{C}$H-CH_2NO_2), 53.82 (C_2-$O\underline{C}H_3$).

HRMS (EI) [$MH^{+\cdot}$] calcud for $C_{12}H_{12}N_2O_4$ = 249.2442, found 249.1500.

HRMS (EI) [$MH^{-\cdot}$] calcud for $C_{12}H_{12}N_2O_4$ = 247.2442, found 247.1000.

b) 1-(2,6-Dimethoxy-quinolin-3-yl)-2-nitro-ethanol **(4b):**

Pale yellow crystals, yield = 89%, R_f = 0.2 (ethyl acetate/petroleum ether: 1/9), M.p = 132-134 °C. IR (ATR) ν cm^{-1}: 3500 (OH), 2958 (aliphatic CH), 1616 (aromatic C=C), 1551 (NO_2), 1229 (C-O). ^{1}H NMR (400 MHz, $CDCl_3$) δ (ppm): 8.07 (s, 1H, H_4), 7.75 (d, *J* = 9.1 Hz, 1H, H_8), 7.29 (dd, *J* = 9.1, 2.8 Hz , 1H, H_7), 7.05 (d, *J* = 2.8 Hz, 1H, H_5), 5.64 (ddd, *J* = 9.2, 6.0, 2.8, Hz, 1H, C<u>H</u>OH), 4.79 (dd, *J*= 13.3, 2.9 Hz, 1H, H_a, $NO_2C\underline{H}_2$), 4.54 (dd, *J* = 13.3, 9.1 Hz, 1H, H_b, $NO_2C\underline{H}_2$), 4.09 (s, 3H, C_2-$OC\underline{H}_3$), 3.89 (s, 3H, C_6-$OC\underline{H}_3$), 3.38 (d, *J* = 5.7 Hz, 1H, OH). ^{13}C NMR (101 MHz, $CDCl_3$) δ (ppm): 157.15 (C_2), 156.54 (C_6),

141.57 (C_{8a}), 135.20 (C_4), 128.31 (C_8), 125.65 (C_{4a}), 122 (C_3), 121.79 (C_7), 106.34 (C_5), 79.49 ($\underline{C}H_2NO_2$), 67.19 (HO-$\underline{C}$H-CH_2NO_2), 55.56 (C_2-O$\underline{C}H_3$), 53.65 (C_6-O$\underline{C}H_3$).

HRMS (EI) [$MH^{+\cdot}$] calcud for $C_{13}H_{14}N_2O_5$ = 279.2602, found 279.150.

HRMS (EI) [$MH^{-\cdot}$] calcud for $C_{13}H_{14}N_2O_5$ = 277.2602, found 277.150.

c) 1-(2-Ethoxy-quinolin-3-yl)-2-nitro-ethanol **(4c):**

White crystals, yield = 79%, R_f = 0.33(ethyl acetate/petroleum ether: 1/9), M.p = 144-146 °C. IR (ATR) ν cm^{-1}: 3350 (OH), 2984 (aliphatic CH), 1624 (aromatic C=C), 1544 (NO_2), 1244 (C-O). ^{1}H NMR (400 MHz, $CDCl_3$) δ (ppm): 8.18 (s, 1H, H_4), 7.83 (d, *J* = 7.7 Hz, 1H, H_8), 7.74 (d, *J* = 7.3 Hz, 1H, H_5), 7.63 (t, *J* = 6.3 Hz, 1H, H_7), 7.41 (t, *J* = 6.5 Hz, 1H, H_6), 5.67 (m, 1H, C$\underline{H}$OH), 4.82 (d, *J* = 12.9, Hz, 1H, H_a, $NO_2C\underline{H}_2$), 4.57 (m, 2H, O$\underline{CH}_2$-CH_3), 4.56 (d, *J* = 13.3 Hz, 1H, H_b, $NO_2C\underline{H}_2$), 3.30 (d, *J* = 4.3 Hz, 1H, OH), 1.47 (t, *J* = 5.8 Hz, 3H, $OCH_2C\underline{H}_3$). ^{13}C NMR (101 MHz, $CDCl_3$) δ (ppm): 158.16 (C_2), 146.23 (C_{8a}), 136.12 (C_4), 130 (C_7), 127.70 (C_5), 127.01 (C_8), 124.92 (C_{4a}), 124.61 (C_6), 121.91 (C_3), 79.54 ($\underline{C}H_2NO_2$), 67.23 (HO-$\underline{C}$H-CH_2NO_2), 62.3 (C_2-O$\underline{C}H_2CH_3$), 14.57 (C_2-$OCH_2\underline{C}H_3$).

HRMS (EI) [$MH^{+\cdot}$] calcud for $C_{13}H_{14}N_2O_4$ = 263.2608, found 263.150.

HRMS (EI) [$MH^{-\cdot}$] calcud for $C_{13}H_{14}N_2O_4$ = 261.2608, found 261.150.

d) 1-(6-Methyl-2-propoxy-quinolin-3-yl)-2-nitro-ethanol **(4d):**

White crystals, yield = 92%, R_f = 0.39 (ethyl acetate/petroleum ether: 1/9), M.p = 106-108 °C. IR (ATR) ν cm^{-1}: 3420 (OH), 2968 (aliphatic CH), 1616 (aromatic C=C), 1545 (NO_2), 1251 (C-O). ^{1}H NMR (400 MHz, $CDCl_3$) δ (ppm): 8.07 (s, 1H, H_4), 7.72 (d, *J* = 8.5 Hz, 1H, H_8), 7.49 (s, 1H, H_5), 7.46 (dd, *J* = 8.5, 1.9 Hz, 1H, H_7), 5.56 (ddd, *J* = 8.8, 5.4, 2.9 Hz, 1H, C$\underline{H}$OH), 4.79 (dd, *J* = 13.3, 2.9 Hz, 1H, H_a, $NO_2C\underline{H}_2$), 4.55 (dd, *J* = 13.1, 9.0 Hz, 1H, H_b, $NO_2C\underline{H}_2$), 4.48 (dt, *J* = 6.6, 3.4 Hz, 2H, O$\underline{CH}_2$-CH_2-CH_3), 3.38 (d, *J* = 5.6 Hz, 1H, O$\underline{H}$), 2.48 (s, 3H, C_6-$C\underline{H}_3$), 1.87 (sept, *J* = 6.8 Hz, 2H, OCH_2-$C\underline{H}_2$-CH_3), 1.07 (

t, *J* = 7.4 Hz, 3H, OCH_2-CH_2-$C\underline{H}_3$). ^{13}C NMR (101 MHz, $CDCl_3$) δ (ppm): 157.89 (C_2), 144.51 (C_{8a}), 135.54 (C_4), 134.27 (C_6), 132.06 (C_7), 126.80 (C_8), 126.66 (C_5), 124.88 (C_3), 121.84 (C_{4a}), 79.65 ($\underline{C}H_2NO_2$), 67.95 (C_2-$O\underline{C}H_2$), 67.37(HO-$\underline{C}$H-CH_2NO_2), 22.29 (OCH_2-$\underline{C}H_2$-CH_3), 21.28 (C_6-$\underline{C}H_3$), 10.74(OCH_2-CH_2-$\underline{C}H_3$).

HRMS (EI) [$MH^{+\cdot}$] calcud for $C_{15}H_{18}N_2O_4$ = 291.3139, found 291.200.

HRMS (EI) [$MH^{-\cdot}$] calcud for $C_{15}H_{18}N_2O_4$ = 289.3139, found 289.150.

e) 1-(2-Methoxy-8-methyl-quinolin-3-yl)-2-nitro-ethanol **(4e):**

White crystals, yield = 79%, R_f = 0.39 (ethyl acetate/petroleum ether: 1/9), M.p = 92-94 °C. IR (ATR) ν cm^{-1}: 3400 (OH), 2917 (aliphatic CH), 1627 (aromatic C=C), 1545 (NO_2), 1249 (C-O). ^{1}H NMR (400 MHz, $CDCl_3$) δ (ppm): 8.12 (d, *J* = 0.8 Hz, 1H, H_4), 7.58 (d, *J* = 8,1 Hz, 1H, H_5), 7.50 (d, *J* = 6.8 Hz, 1H, H_7), 7.31 (d, *J* = 7.7 Hz, 1H, H_6), 5.65 (ddd, *J* = 9.2, 5.6, 2.8, Hz, 1H, C$\underline{H}$OH), 4.79 (dd, *J* = 13.3, 2.9 Hz, 1H, H_a, $NO_2C\underline{H}_2$), 4.55 (dd,1H, *J* = 13.3,9.1 Hz, 1H, H_b, $NO_2C\underline{H}_2$), 4.13 (s, 3H, C_2-$OC\underline{H}_3$), 3.29 (d, *J* = 5.8 Hz, 1H, O$\underline{H}$), 2.69 (s, 3H, C_8-$C\underline{H}_3$). ^{13}C NMR (101 MHz, $CDCl_3$) δ (ppm): 157.49 (C_2), 144.94 (C_{8a}), 136.43 (C_4), 135.22 (C_8), 130.24 (C_7), 125.53 (C_5), 124.84 (C_{4a}), 124.37 (C_6), 121.3(C_3), 79.49 ($\underline{C}H_2NO_2$), 67.16 (HO-$\underline{C}$H-CH_2NO_2), 53.56 (C_2-$O\underline{C}H_3$), 17.60 (C_8-$\underline{C}H_3$).

HRMS (EI) [$MH^{+\cdot}$] calcud for $C_{13}H_{14}N_2O_4$ = 263.2607, found 263.150.

HRMS (EI) [$MH^{-\cdot}$] calcud for $C_{13}H_{14}N_2O_4$ = 261.2607, found 261.150.

f) 1-(2-Ethoxy-6,7-dimethy-quinolin-3-yl)-2-nitro-ethanol **(4f):**

White crystals, yield = 82%, R_f = 0.36 (ethyl acetate/petroleum ether: 1/9), M.p = 142-144 °C. IR (ATR) ν cm^{-1}: 3410 (OH), 2978 (aliphatic CH), 1617 (aromatic C=C), 1541 (NO_2), 1243 (C-O). ^{1}H NMR (400 MHz, $CDCl_3$) δ (ppm): 8.01 (s, 1H, H_4), 7.59 (s, 1H, H_8), 7.44 (s, 1H, H_5), 5.60 (ddd, *J* = 7.6, 3.9 Hz, 1H, C$\underline{H}$OH), 4.76 (dd, *J* = 13.1, 3.0 Hz, 1H, H_a, $NO_2C\underline{H}_2$), 4.56 (dd, *J* = 13.1, 9.2 Hz, 1H, H_b,

$NO_2C\underline{H}_2$), 4.53 (q, *J* = 1.6 Hz, 2H, $OC\underline{H}_2$-CH_3), 3.34 (d, *J* = 5.5 Hz, 1H, O<u>H</u>), 2.41 (s, 3H, C_7-$C\underline{H}_3$), 2.38 (s, 3H, C_6-$C\underline{H}_3$), 1.44 (t, 3H, $OCH_2C\underline{H}_3$). ^{13}C NMR (101 MHz, $CDCl_3$) δ (ppm): 157.84 (C_2), 145.04 (C_{8a}), 140.21 (C_7), 135.24 (C_4), 134.11 (C_6), 127.13 (C_5), 126.67 (C_8), 123.33 (C_{4a}), 120.77 (C_3), 79.64 ($\underline{C}H_2NO_2$), 67.44 (HO-<u>C</u>H-CH_2NO_2), 62.06 (C_2-O<u>C</u>H_2CH_3), 20.33 (C_7-<u>C</u>H_3), 19.71 (C_6-<u>C</u>H_3), 14.88 ($OCH_2\underline{C}H_3$).

HRMS (EI) [$MH^{+\cdot}$] calcud for $C_{15}H_{18}N_2O_4$ = 291.3139, found 291.200.

HRMS (EI) [$MH^{+\cdot}$] calcud for $C_{15}H_{18}N_2O_4$ = 289.3139, found 289.150.

***g) 1-(2-Methoxy-6-methyl-quinolin-3-yl)-2-nitro-ethanol* (4g):**

White crystals, yield = 78%, R_f = 0.32 (ethyl acetate/petroleum ether: 1/9), M.p = 122-124 °C. IR (ATR) ν cm^{-1}: 3400 (OH), 2939 (aliphatic CH), 1619 (aromatic C=C), 1545 (NO_2), 1248 (C-O). ^{1}H NMR (400 MHz, $CDCl_3$) δ (ppm): 8.07 (s, 1H, H_4), 7.74 (d, *J* = 8.4 Hz, 1H, H_8), 7.49 (s,1H, H_5), 7.46 (dd, *J* = 8.8, *J* = 2 Hz, 1H, H_7), 5.63 (ddd, *J* = 8.6, 4.2, 2.5 Hz, 1H, C<u>H</u>OH), 4.77 (dd, *J* = 13.3, 2.9 Hz, 1H, H_a, $NO_2C\underline{H}_2$), 4.54 (dd, *J* = 13.3, 9.1 Hz, 1H, H_b $NO_2C\underline{H}_2$), 4.10 (s, 3H, C_2-$OC\underline{H}_3$), 3.39 (d, *J* = 5.7 Hz, 1H, OH), 2.48 (s, 3H, $C\underline{H}_3$). ^{13}C NMR (101 MHz, $CDCl_3$) δ (ppm): 158.06 (C_2), 144.4 (C_{4a}), 135.65 (C_4), 134.4 (C_{8a}), 132.12 (C_8), 126.82 (C_5), 126.67 (C_7), 124.98 (C_6), 121.8 (C_3), 79.51 ($\underline{C}H_2NO_2$), 67.10 (HO-<u>C</u>H-CH_2NO_2), 53.70 (C_2-O<u>C</u>H_3), 21.29 (C_6-<u>C</u>H_3).

***h) 1-(2-Methoxy-6,7-dimethyl-quinolin-3-yl)-2-nitro-ethanol* (4h):**

White crystals, yield = 76%, R_f = 0.31 (ethyl acetate/petroleum ether: 1/9), M.p = 152-154 °C. IR (ATR) ν cm^{-1}: 3400 (OH), 2920 (aliphatic CH), 1622 (aromatic C=C), 1546 (NO_2), 1248 (C-O). ^{1}H NMR (400 MHz, $CDCl_3$) δ (ppm): 8.04 (s, 1H, H_4), 7.63 (s, 1H, H_8), 7.47 (s, 1H, H_5), 5.62 (ddd, *J* = 8.0, 4.8, 2.8 Hz, 1H, C<u>H</u>OH), 4.77 (dd, *J* = 13.3, 2.9 Hz, 1H, H_a, $NO_2C\underline{H}_2$), 4.55 (dd, *J* = 13.3, 9.1 Hz, 1H, H_b, $NO_2C\underline{H}_2$), 4.10 (s, 3H, C_2-$OC\underline{H}_3$), 3.27 (d, *J* = 5.8 Hz, 1H, O<u>H</u>), 2.42 (s, 3H, C_7-$C\underline{H}_3$), 2.39 (s,

3H, C_6-C<u>H</u>$_3$). ^{13}C NMR (101 MHz, $CDCl_3$) δ (ppm): 158.14 (C_2), 145.01 (C_{8a}), 140.29 (C_7), 135.33 (C_4), 134.24 (C_6), 127.15 (C_5), 126.71 (C_8), 123.43 (C_{4a}), 120.71 (C_3), 76.56 (<u>C</u>H$_2$NO$_2$), 67.27 (HO-<u>C</u>H-CH$_2$NO$_2$), 53.62 (C_2-O<u>C</u>H$_3$), 20.34 (C_7-<u>C</u>H$_3$), 19.73 (C_6-<u>C</u>H$_3$).

HRMS (EI) [$MH^{+\cdot}$] calcud for $C_{14}H_{16}N_2O_4$ = 277.3158, found 277.150.

HRMS (EI) [$MH^{-\cdot}$] calcud for $C_{14}H_{16}N_2O_4$ = 275.3158, found 275.150.

i) 1-(2,7-Dimethoxy-quinolin-3-yl)-2-nitro-ethanol **(4i):**

White crystals, yield = 70%, R_f = 0.21 (ethyl acetate/petroleum ether: 1/9), M.p = 146-148 °C. IR (ATR) ν cm^{-1}: 3150 (OH), 2966 (aliphatic CH), 1620 (aromatic C=C), 1548 (NO_2), 1218 (C-O). ^{1}H NMR (400 MHz, $CDCl_3$) δ (ppm): 8.10 (s, 1H, H_4), 7.63 (d, *J* = 8.8 Hz, 1H, H_5), 7.22 (dd, *J* = 2.5 Hz, 1H, H_8), 7,06 (dd, *J* = 8.8, 2.5 Hz, 1H, H_6), 5.65 (ddd, *J* = 9.0, 5.8, 2.9 Hz, 1H, C<u>H</u>OH) 4.78 (dd, *J* = 13.3, 2.9 Hz, 1H, H_a, NO$_2$C<u>H</u>$_2$), 4.57 (dd, *J* = 13.3, 9.1 Hz, 1H, H_b, NO$_2$C<u>H</u>$_2$), 4.13 (s, 3H, C_2-OC<u>H</u>$_3$), 3.94 (s, 3H, C_7-OC<u>H</u>$_3$), 3.19 (d, *J* = 5.8 Hz, 1H, OH). ^{13}C NMR (101 MHz, $CDCl_3$) δ (ppm): 161.48 (C_7), 159.03 (C_2), 148.07 (C_{8a}), 135.91 (C_4), 128.74 (C_5), 119.79 (C_3), 118.94 (C_{4a}), 116.99 (C_8), 106.10 (C_6), 79.57 (<u>C</u>H$_2$NO$_2$), 67.16 (HO-<u>C</u>H-CH$_2$NO$_2$), 55.52 (C_7-O<u>C</u>H$_3$), 53.72 (C_2-O<u>C</u>H$_3$).

HRMS (EI) [$MH^{+\cdot}$] calcud for $C_{13}H_{14}N_2O_5$ = 279.2602, found 279.150.

HRMS (EI) [$MH^{-\cdot}$] calcud for $C_{13}H_{14}N_2O_5$ = 277.2602, found 277.150.

2.2. Micro-organisms

Five microbial strains were included in this study; *Staphylococcus aureus* ATCC 25923, *Pseudomonas aeruginosa* ATCC 1117, *Escherichia coli* ATCC 25922, and fungal strain *Candida albicans* ATCC 90029. Additionally, a clinical strain of vancomycin-resistant *Enterococcus faecium* was also part of the investigation.

2.3.Anti-microbial activity

The antimicrobial properties of the title compounds (**4a**-**4i**) were evaluated against five microbial strains, including two Gram-negative bacteria (*Pseudomonas aeruginosa* ATTC 1117 and *Escherichia coli* ATCC 25922), two Gram-positive bacteria (*Staphylococcus aureus* ATCC 25923 and a clinical strain of vancomycin-resistant *Enterococcus faecium*), as well as a fungal strain (*Candida albicans* ATCC 90029). An initial assessment of antimicrobial activity followed the guidelines provided by the Clinical and Laboratory Standards Institute (CLSI). The disc diffusion method was employed on Mueller Hinton agar plates, while for the fungal strain, Mueller Hinton-glucose-methylene blue agar plates were used (http://em100.edaptivedocs.net/Login.aspx). Each compound was solubilized in dichloromethane, and sterile empty paper discs were impregnated with 20 µl of the solution to reach a final concentration of 100 µg per disc. The discs were allowed to dry at room temperature for one hour. The designated strains were cultured overnight at 37°C on nutrient agar plates. Subsequently, microbial suspensions were prepared in sterile saline at a density of 0.5 MacFarland and used to swab the surfaces of Mueller Hinton plates. The previously prepared discs were then deposited. The experiments were replicated three times, with Ciprofloxacin as a positive control and dichloromethane-impregnated discs as a negative control. The plates were incubated aerobically overnight at 37°C, and then inhibition zone diameters were measured. Compounds with the most significant inhibition zone diameters were subjected to the measurement of the minimal inhibition concentrations (MIC) by the broth microdilution method. Experiments were conducted in duplicates using Mueller Hinton broth II following the recommendations of the CLSI.

2.3. Computational methods

The structures of the synthesized compounds (**4a**-**4i**) were drawn using the Chem-Draw 12.0 tool. The molecular geometries were optimized, and the energy of each molecule was minimized under gas-phase conditions in their neutral states. This process was accomplished using the Density Functional Theory (DFT) method, specifically employing Becke's three-parameter hybrid exchange functional known as B3LYP [34], in combination with the Lee-Yang-Parr correlation functional [35]. The Triple Zeta

polarized (TZP) basis set implemented in the AMS program [36] was used. Vibrational frequencies were calculated at the same level as the optimization, except for the **4i** compound, several computational functionals were considered, including two Generalized Gradient Approximation methods (PBE gradient-corrected exchange-correlation functional of Perdew-Burke-Ernzerhof [37] and the BLYP exchange-correlation functional by Becke [38] and Lee, Yang, and Parr [39]), two well-established hybrid functionals (B3LYP [40], PBE0 [41]), and two range-separated functionals (CAMY-B3LYP, CAM-B3LYP [42]), with the TZP basis set [36]. Quantum Bader Atom In Molecule (QTAIM) [43,44], Molecular Electrostatic Potential (MEP) [45–48], and global reactivity descriptors, such as ionization potential, electrophilicity, and net electrophilicity, are also exhibited through HOMO and LUMO energies. The Total Density of States (TDOS) for all compounds was investigated using the AMS program [36] and the corresponding plots were generated with OriginPro software [49].

2.4. Molecular Docking Study

To assess the interaction between synthesized molecules and the target protein, we conducted a molecular docking study using AutoDockVina 4.2 (MGLTools 1.5.7) [50]. The study involved optimized structures of nitroaldol quinoline derivatives and the standard molecule Ciprofloxacin, formatted as a pdb file through the Open Babel GUI tool [51]. The crystal structure of DNA-gyrase with PDB ID 1KZN was chosen as the protein model, obtained from the RSC Protein Data Bank (http://www.rcsb.org). Initial validation of the molecular docking protocol included re-docking the co-crystallized ligand (Clorobiocin) into the active site of DNA-gyrase. The PyMol software [52] as then used to calculate the RMSD (Root-Mean-Square Deviation) value for validation. Protein preparation involves eliminating water molecules, adding polar hydrogen atoms, assigning Kollman charges, and consolidating non-polar hydrogen atoms. The protein carried a Kollman charge of -47.066. The grid dimensions were set at 40 Å with a grid spacing of 0.500 Å, centered on X: 18.533, Y: 30.3898, Z: 50.110 Å. The grid included amino acid residues Ala, Arg, Asn, Asp, Cys, Gln, Glu, Gly, Ile, Leu, Met, Pro, Ser, Thr, and Val. The predicted active site volume

for the receptor was 18.43 Å^3. Docking poses of the ligands with the receptors were explored using the Lamarckian Genetic Algorithm. For optimal binding affinity assessment, AutoDock 4.0 generated nine poses. Subsequently, the best binding energy pose underwent further analysis using BIOVIA Discovery Studio 2021 (BIOVIA) (https://discover.3ds.com/discovery-studio-visualizer-download).

2.5. Generation

The chemical structure of nine lead compounds, unless specified otherwise, was provided in the form of a canonical simplified molecular input line entry system (SMILES) notation. This was done to assess various *in silico* pharmacokinetic parameters. The SMILES representations of these compounds were generated using the Open Babel GUI tool [51].

2.6. SwissADME online server

In silico SwissADME tool (http://www.swissadme.ch/) was employed to predict some physicochemical properties, pharmacokinetics, and drug-likeness profile for the lead compounds.

3. Results and discussion

3.1. Chemical study

The synthesis of the title compounds, referred to as **4a**-**4i**, involved four primary steps following the reaction sequences detailed in (Scheme 1). In the initial stage, acetanilide derivatives (**1**) were generated through the acetylation of anilines in a mixture of acetic anhydride and acetic acid. In the second step, 2-chloroquinolines-carbaldehyde (**2**) was prepared by treating acetanilide (**1**) with Vilsmeier–Haack reagent ($POCl_3$ in DMF) following the Meth-Cohn method [53]. The third step involved substituting the chlorine at position 2 of quinoline with suitable nucleophiles. This was achieved by refluxing substituted 2-chloro-3-formyl quinolines in DMF with the appropriate nucleophilic reagents in a basic medium [54] to prepare 2-alkoxyquinolines-3-carbaldehyde (**3**).

The last step consisted of condensing the alkoxyquinolines, 2-alkoxyquinoline-3-carbaldehyde derivatives, with nitromethane in a mixture of ethanol and methanol at 0°C for 2h. FTIR, mass spectrometry, ^{1}H NMR, and ^{13}C NMR were used to characterize the compounds (**4**), obtained in good yields.

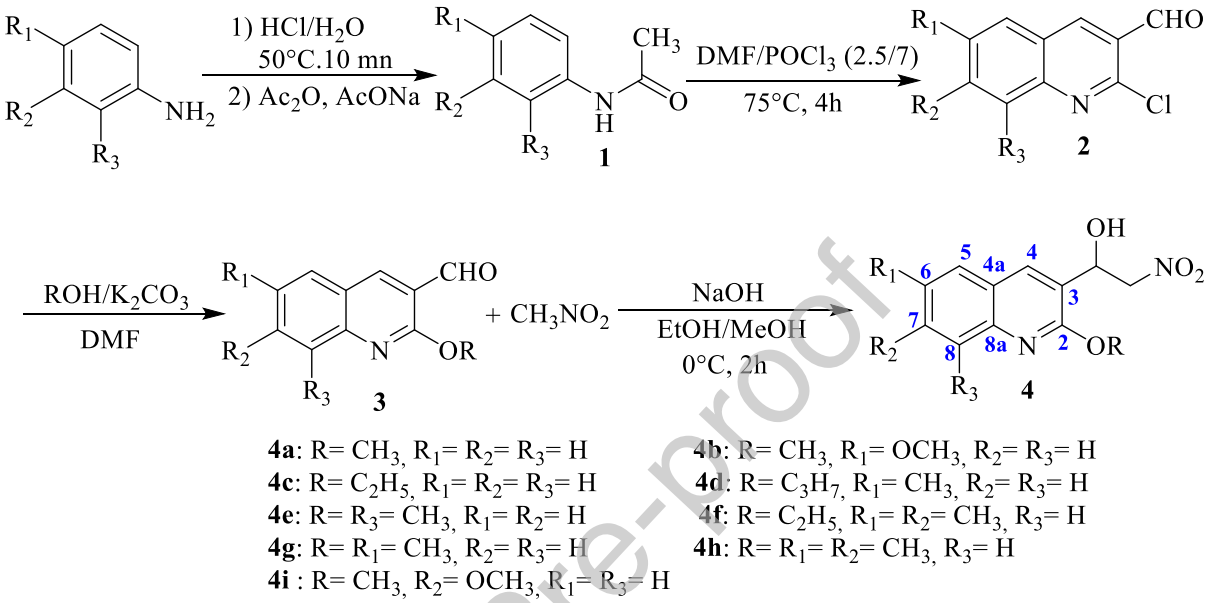

Scheme 1. Synthesis of the new Nitroaldol Quinoline Derivatives (**4a-4i**).

In the ^{1}H NMR spectra, the proton of the hydroxyl group for **4a** was observed at δ 3.31 ppm as a doublet with a coupling constant of ^{2}J = 5.6 Hz. The protons of the methoxy group CH_3O at C_2 (quinoline) appear at δ= 4.13 ppm as an intense singlet. Two sets of diastereotopic protons of CH_2 are observed in the spectrum, appearing at δ= 4.55 ppm (split into a doublet of doublets with coupling constants of 9.1 and 13.4 Hz) and δ= 4.79 ppm (also split into a doublet of doublets with coupling constants of 2.8 and 13.4 Hz). Additionally, the proton associated with the asymmetric carbon resonates at δ= 5.66 ppm, presenting as a complex signal (doublet of doublets of doublets), with three distinct coupling constants of J = 2.8, 5.2, and 8.4 Hz. The aromatic protons appear between δ= 7.41 ppm and δ= 8.18 ppm. The ^{13}C NMR spectrum for **4a** shows the presence of methoxy carbon at δ= 53.82 ppm and a signal at δ= 67.01 ppm corresponding to the asymmetric carbon, the chemical shift appears at δ = 79.45 ppm characterizes the methylene carbon CH_2–NO_2. The

region between δ= 121.87 and 158.48 ppm is assignable to the aromatic carbons. Additionally, the mass spectrum analysis shows a peak at *m/z* 249.150 [M+], which corresponds to its molecular formula $C_{12}H_{12}N_2O_4$. The detailed procedure and analytical data for all the derivatives (**4a**–**4i**) are provided in the experimental section.

3.2. Biological study

In terms of antibacterial activity, all our compounds were inactive against Gram-negative bacterial strains. However, with the exception of **4f**, all the molecules exhibited antibacterial activity against Gram-positive bacteria, with mean inhibition zone diameters ranging between 9.33 mm and 29.33 mm. On the other hand, all the compounds showed antifungal activities against *Candida albicans*, with mean inhibition zone diameters ranging between 6.33 mm and 22 mm. The results of the antimicrobial activity testing are presented in (Table 1). Compounds **4a**, **4g**, **4b**, **4i**, and 4**e** showed promising activity against the fungal strain and Gram-positive bacteria, especially the vancomycin-resistant *E. faecium* strain, where the inhibition zone diameters were larger than those shown with the positive control (Ciprofloxacin).

Table 1: Inhibition zone diameters of synthesized compounds (**4a-4i**) in mm (mean±SD)

Compounds	**Inhibition zone (mm)**				
	Fungi	**Gram-positive bacteria**		**Gram-negative bacteria**	
	C. albicans	***S. aureus***	***E. faecium* vanco-R**	***E. coli***	***P. aeruginosa***
4a	22.00 ± 2.65	29.33 ± 0.58	29.00 ± 1.73	-	-
4g	16.66 ± 0.58	18.67 ± 1.15	20.67 ± 1.15	-	-
4b	14.66 ± 1.53	21.00 ± 1.00	23.00 ± 2.65	-	-
4i	17.66 ± 2.31	18.00 ± 1.73	19.33 ± 0.58	-	-
4e	17.66 ± 0.58	26.00 ± 3.46	26.00 ± 1	-	-
4h	13.66 ± 2.08	9.33 ± 3.21	14.67 ± 0.58	-	-
4c	11.66 ± 1.53	17.00 ± 11.27	12.00 ± 3.61	-	-
4f	8.66 ± 0.58	-	-	-	-
4d	6.33 ± 5.69	14.00 ± 1	12.67 ± 1.15	-	-
Ciprofloxacin	-	45	20	34	38

(-) No observable areas of inhibition surrounding the discs.

Among the selected compounds for MIC measurement, **4e** was the most active molecule with a MIC of 25 µg/ mL against the three microbial strains. The other compounds showed MICs ranging between 25 µg/ mL and > 100 µg/ mL, as shown in (Table 2).

Table 2: Minimal inhibition concentrations of selected synthesized compounds in µg/ mL.

Product	*C. albicans*	*S. aureus*	*E. faecium* vancomycin Resistant
4a	50	> 100	100
4g	25	100	50
4e	25	25	25
4b	-	> 100	> 100
4i	50	100	100
Ciprofloxacin	-	2	8

Significant activity relationships were identified by analyzing the anti-microbial results presented in (Tables 1 and 2). Notably, as the alkoxyl carbon chain in position 2 increased, there was a decline in anti-microbial activity. This decrease is attributed to steric hindrance near the nitro function, affecting the enzyme binding site. Interestingly, this observation aligns well with the QTAIM analysis, which highlights the formation of a carbon-hydrogen bond involving the propyl group in the **4d** compound. Compared with a previous study of chlorine-substituted analogs reported by Zoltän Cziäky et al. [55], compounds substituted with methoxy in position 2 exhibited greater anti-fungal activity. The addition of a methyl group to the benzyl ring (at positions 6 or 6 and 7) reduces the anti-microbial activity, as well as the methoxy substitution (at positions 6 and 7). Remarkably, methyl in position 8 gives the best results in this evaluation, similar to the fluoroquinolones [56].

3.3.Computational Investigations

3.3.1. Analysis of Molecular Orbitals and Total Density of State (TDOS)

Analyzing and understanding the composition of frontier molecular orbitals is of paramount importance in predicting reactivity behaviors. These orbitals play a pivotal role in monitoring interactions between chemical species by identifying the orbitals responsible for donor-acceptor interactions, such as HOMO-

LUMO interactions, and determining which molecular orbitals contribute to specific bonding or non-bonding interactions. Additionally, they have a direct relation with the global reactivity descriptors (see § .3.3.3). The results obtained from the geometry optimization of the present structures show that the HOMO is centered at the quinoline donor region with combined p (C=C) and p* (C=N) characters. The LUMO orbital is centered at the -NO_2 acceptor group with combined N=O and N-O with a p and p* characters, respectively. The localization of the HOMO and LUMO orbitals is very similar for all the studied compounds. Therefore, we have chosen to present only the density distribution of the **4a** molecule (Fig. 1), while the distributions for **4b** to **4i** are provided in the supplementary materials.

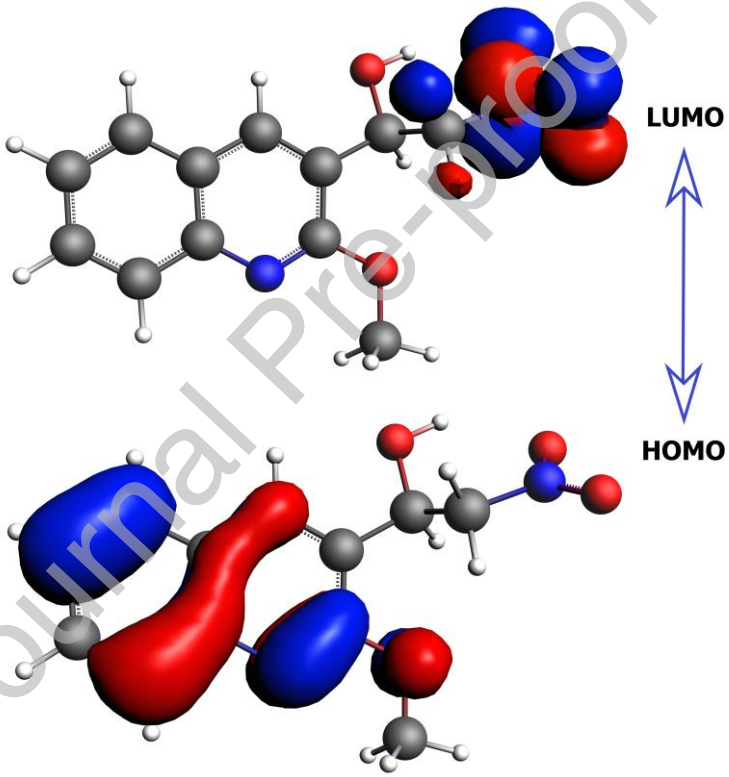

Fig. 1. HOMO and LUMO molecular orbital for **4a** compound.

For a better understanding of the reactivity and electronic properties of the synthesized compounds, total density of state (TDOS) plots were calculated and analyzed. The energy gap values and energy levels for all the synthesized molecules are plotted in (Fig. 2). The TDOS plots show a significant shift in the

occupied orbital of **4b** compared to the other compounds, confirming that electron transfer is more important in this case. This aligns well with the calculated maximal charge acceptance value (indicating that **4b** presents the highest value of ΔN_{max} = 1.213). In addition, it has a moderate energy gap of 3.537 eV attributed to its chemical reactivity, while **4i** recorded the highest energy gap of 4.047 eV. Moreover, both HOMO and LUMO are almost spread over the entire molecules. The separation is minimized in **4b**, **4f**, **4d**, **4h**, **4e**, and **4g**, with a gap varying from 3.5 to 3.8 eV. The HOMO density is predominantly associated with the quinoline unit and donor groups (oxygen atoms, methoxy, methyl, etc.), suggesting that electrophilic attacks can occur mostly at these sites. Conversely, the LUMO density is primarily influenced by the presence of the shared nitro group, indicating a higher probability of nucleophilic attacks at these sites. This has been confirmed by the MEP surfaces.

Whenever the number of carbons is high in the radical (**R**) (refer to Scheme 1 in the supplementary materials), the donor inductive effect increases, enriching the quinoline cycle with electrons and consequently reducing the energy gap. This phenomenon is evident in pairs such as (**4a**, **4c**), (**4g**, **4d**), and (**4h**, **4f**). According to the results, compound **4b** has the smallest energy gap value due to the donor mesomeric effect of the -OCH_3 group at position 6. In contrast, compound **4i** has the largest energy gap value because of the attractive inductive effect of -OCH_3 at position **7**, depleting the quinoline cycle of electrons and increasing the gap.

In cases where the cycle is substituted with groups, -CH_3, as seen in compound **4h**, two methyl groups -CH_3 exhibit donor inductive effects. Comparing compounds **4h** and **4g** reveals that the energy gap decreases with an increase in the number of methyl groups -CH_3.

For **4e**, with an energy gap value higher than that of compound **4h** and lower than that of compound **4g**, this is explained by the proximity of the methyl group -CH_3 at position 8 to the nitrogen atom, which is more electronegative than the carbon atom.

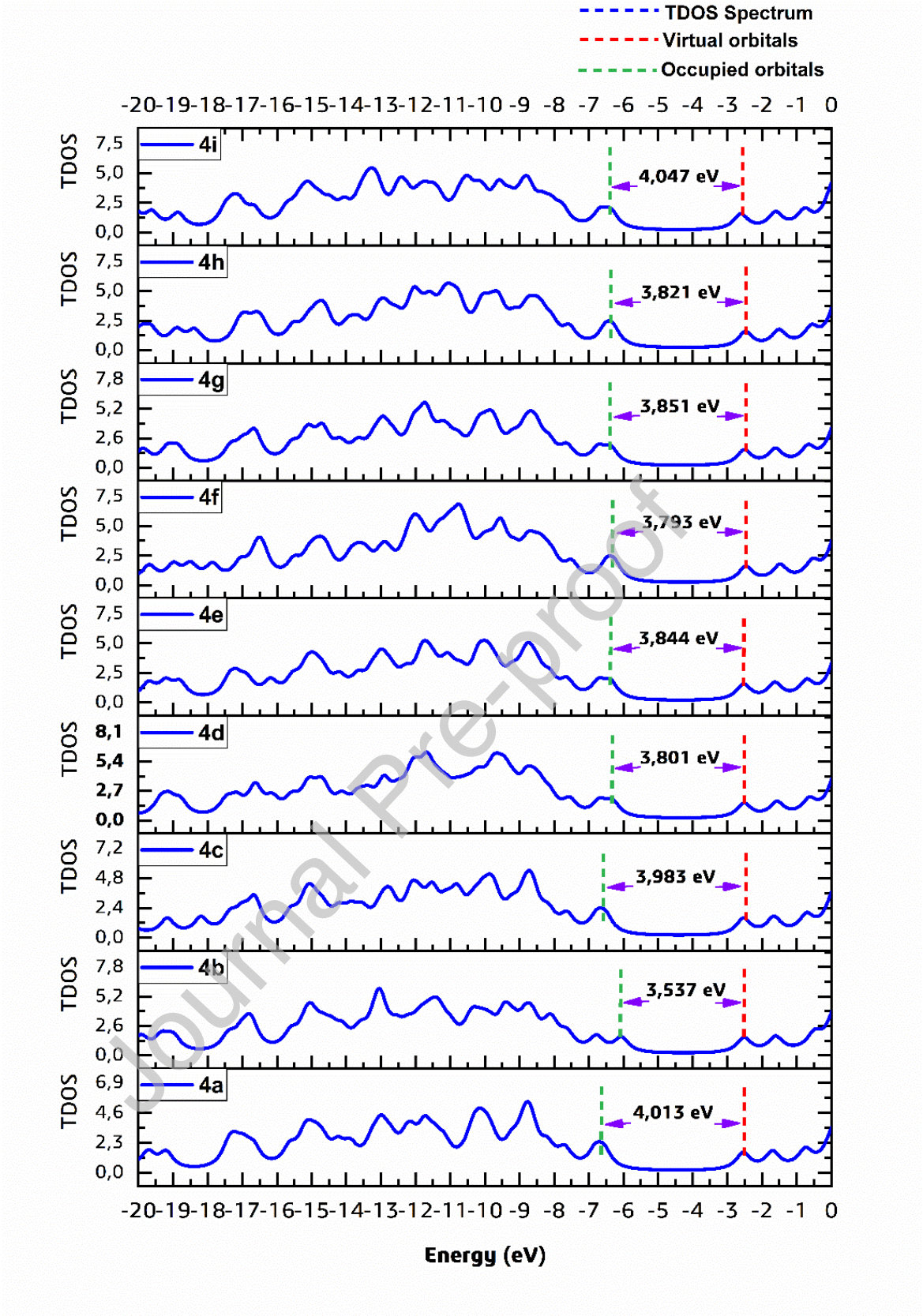

Fig. 2. Total density of state, TDOS for **4a-4i** compounds at B3LYB and TZP basis set.

3.3.2. Vibrational Analysis

The calculated vibrational (Infra-Red) offers valuable insights into the specific vibrational characteristics. These insights are instrumental in deciphering the experimental spectra, which were assessed in the ATR-solid state in our study. The simulated spectra were obtained at the same level as the optimization (using the functional B3LYP and the basis set TZP) because of the significant precision achieved using this hybrid functional compared to the experimental spectrum, and it is crucial to accurately describe the electronic structure and vibrational frequencies of molecules. Meanwhile, in order to prove this point, several functionals were used such as the Generalized Gradient Approximation (PBE, BLYP), hybrid functionals (B3LYP, PBE0), and range-separated functionals (CAMY-B3LYP, CAM-B3LYP), with the TZP basis set [36].The calculated spectra were then compared to the experimental spectrum. Both the experimental and theoretical absorption spectra of **4i** are presented in (Fig. 3), and the selected vibrational frequencies are summarized in the supplementary materials.

The experimental and calculated absorption spectra exhibit close resemblance in terms of their shapes. However, the relative intensity is significantly influenced by the functional class (GGA, hybrid, or range-separated), with hybrid and range-separated functionals showing higher intensity than GGA. Theoretical absorption peaks with frequency values above 3169 cm^{-1} display a significant redshift in range-separated and hybrid spectra (CAM-BLYP, CAMY-BLYP, B3LYP, and PBE0) compared to the experimental spectrum. The respective absorption bands are 3773C cm^{-1}, 3773C cm^{-1}, 3772C cm^{-1}, and 3780C cm^{-1}. Notably, the BLYP, B3LYP, PBE, and PBE0 functionals all exhibit good agreement with the experimental spectrum. However, some discrepancies are observed in specific vibrational modes with BLYP, and slightly higher values are found in certain cases with the hybrid B3LYP functional. The PBE0 functional demonstrates its potential reliability in predicting vibrational modes.

The inclusion of hybrid B3LYP and PBE0 significantly improves theoretical spectra, with even more pronounced improvement using GGA functionals (BLYP, PBE). Range-separated CAM-B3LYP and CAMY-B3LYP, which incorporate empirical dispersion corrections, yield vibrational frequencies slightly

higher than the experimental values (red-shifted), emphasizing the importance of including dispersion interactions in theoretical calculations for accurate vibrational spectrum prediction. Examining specific vibrational modes, the stretching mode of the nitro (O-NO) group at 1620E cm^{-1} consistently shows a redshift across most functionals, with PBE and B3LYP providing the closest match to the experimental value (1622C and 1636C cm^{-1}, respectively). Similarly, the stretching mode of C-O bonds at 1010 cm^{-1} exhibits variations among functionals, with BLYP (1011C cm^{-1}), PBE (1010C cm^{-1}), and B3LYP (1014C cm^{-1}) predicting values closer to the experiment. Due to the significant precision achieved using the hybrid functional B3LYP compared to the experimental spectrum, we chose to conduct our calculations with this particular functional.

The calculated spectra of the compounds **4a-4h** offer valuable insights into their specific vibrational characteristics. The corresponding experimental spectra are assessed in the ATR-solid state (Supplementary material). From results, all the calculated spectra show no imaginary frequencies, theoretically confirming the molecular stability of these derivatives. Comparing the results reveals a substantial level of agreement, except for the OH bonds. The absorption band values between 3448E - 3205E cm^{-1} represents the OH stretching vibrations, with corresponding calculated frequencies falling within the range of 3732C - 3166C cm^{-1}. The C-H stretching vibrations of the synthesized compounds appear in the ranges 3066E - 2954E cm^{-1} and 3032C - 2987C cm^{-1}, values close to those reported in the literature [33]. The most intense band observed in the ranges 1627E - 1615E cm^{-1} refers to the stretching vibration of the nitro (O-NO) group, closely aligned with the calculated range values of 1636C -1614C cm^{-1}. The stretching vibrations of the C=C bonds are assigned in the range 1553E - 1504E cm^{-1} and 1552C - 1497C cm^{-1}. Additionally, the obtained vibrations in the ranges 1466E - 1418E cm^{-1} and 1453 - 1414 cm^{-1} are attributed to the stretching C=N vibrations of the quinoline unit. Experimental peaks in the range of 1384E - 1309E cm^{-1} represent the symmetric and asymmetric bending vibrations of CH_3. In the theoretical spectra, they are located in the range of 1386C - 1221C cm^{-1}, values close to the reported ones [57]. Vibrations in the ranges 1218E - 1144E cm^{-1} / 1222C - 1150C cm^{-1} refer to the symmetric and

asymmetric bending vibrations of C-C bonds. Peaks in 971E - 938E cm^{-1} / 963C - 900C cm^{-1} ranges refer to the in-plane binding vibrations of C-O bands. The in-plane bending vibrations of CH appear in the ranges 792E – 713E cm^{-1} / 803C -668C cm^{-1}, and the corresponding out-of-plane vibrations appear in the ranges 938E - 811E cm^{-1} / 900C - 813C cm^{-1}.

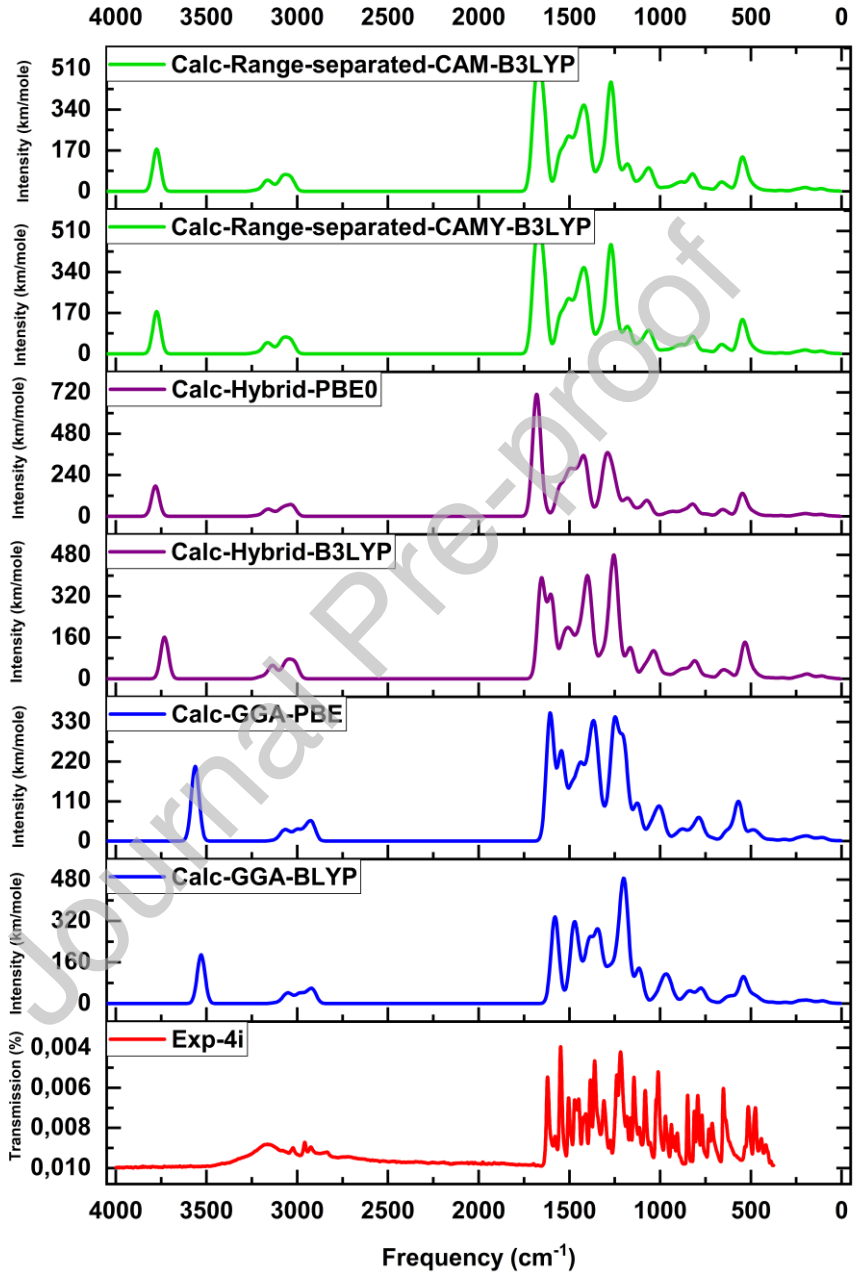

Fig. 3. Experimental (Exp) and simulated (Calc) infrared spectra of the compound 1-(2,7-Dimethoxy-quinolin-3-yl)-2-nitro-ethanol (**4i**).

Vibrational ranges 651E-475E cm^{-1} / 651C-471C cm^{-1} represent the in-plane bending and symmetric out-of-plane bending vibrations of the aromatic C-C-C bonds.

The comparative examination of infrared (IR) spectra for compounds **4a** to **4i** provides a comprehensive insight into the vibrational dynamics within each molecule, highlighting both areas of concurrence and potential enhancements in the B3LYP theoretical model. The comparative spectra of compounds **4a**-**4h** are reported in the supplementary information. Crucially, all computed spectra show the absence of imaginary frequencies, affirming their theoretical molecular stability.

Compound **4a** showcases the model's accuracy in predicting aliphatic CH stretching vibrations, as evidenced by the close alignment between experimental (2949E cm^{-1}) and theoretical (3034C cm^{-1}) values. The concordance extends to nitro group vibrations (stretching O-NO) with values of (1600C cm^{-1} /1627E cm^{-1}), C=C stretching (1510 cm^{-1} / 1548 cm^{-1}), and C=N stretching modes (1459C -1426C cm^{-1} / 1473E - 1440E cm^{-1}), accentuating the reliability of the theoretical predictions. Similarly, Compound **4b** exhibits commendable agreement in aliphatic CH stretching vibrations (3032C - 2990C cm^{-1} /2958E cm^{-1}), stretching O-NO (1603C cm^{-1} / 1615E cm^{-1}), and C=N stretching modes (1451C cm^{-1} / 1447E cm^{-1}), as well as in C=C stretching vibrations (1494C cm^{-1}/1550E -1506E cm^{-1}). Compound **4c** further validates the model's precision in predicting aliphatic CH stretching vibrations (3034C cm^{-1} / 2984E cm^{-1}) and nitro group vibrations (1606C cm^{-1} / 1623E cm^{-1}), with small variation in C=C stretching (1557 cm^{-1} / 1543 - 1500 cm^{-1}) and C=C bending modes (1011C cm^{-1} / 1011E cm^{-1}). Compound **4d** underscores the model's reliability in capturing aliphatic CH stretching (3024C cm^{-1} / 2968E cm^{-1}) and nitro group vibrations (1614C cm^{-1} / 1615E cm^{-1}), with potential adjustments needed for a more accurate representation of C=C stretching (1482C cm^{-1} / 1545E cm^{-1}) and C-O stretching modes (1041C cm^{-1} / 1079E cm^{-1}). Compound **4e** reveals a nuanced scenario with satisfactory agreement in aliphatic CH stretching (3030C cm^{-1} / 2917E cm^{-1}) and nitro group vibrations (1600C cm^{-1}/1627E cm^{-1}) but indicates potential disparities in the representation of C=C stretching (1488C cm^{-1}/1583E – 1545E cm^{-1}) and C=C bending modes (1182C cm^{-1} / 1273E - 1627E cm^{-1}). Compound **4f** demonstrates precision in predicting aliphatic CH stretching

(3094C - 3007C cm^{-1} / 2978E cm^{-1}) and nitro group vibrations (1611C cm^{-1} / 1617E cm^{-1}) but reveals notable discrepancies in the representation of symmetric and asymmetric C-C bending modes (1175C cm^{-1} / 1243E – 1207E cm^{-1}). Compound **4g** showcases the model's adeptness in predicting various vibrational modes, including aliphatic CH stretching (3025C cm^{-1} / 2939E cm^{-1}), nitro group vibrations (1603C cm^{-1} /1619E cm^{-1}), and C=N stretching (1466C – 1396C cm^{-1} /1449E cm^{-1}), while indicating potential refinements in the representation of C-C bending modes (1184C cm^{-1} / 1248E – 1126E cm^{-1}). Compound **4h** highlights areas of agreement in aliphatic CH stretching (3007C cm^{-1} / 2920E cm^{-1}), nitro group vibrations, and in-plane bending C-H (793C cm^{-1} / 776E – 707E cm^{-1}), with notable disparities in C-C bending modes (1175C cm^{-1} / 1247E – 1144E cm^{-1}). Finally, compound **4i** reveals a noteworthy discrepancy in the OH stretching mode (3531C cm^{-1} /3169E cm^{-1}), underscoring the need for refinement in this area. The model's overall precision is evident in aliphatic CH stretching (2926C – 2950C cm-1/ 2954E – 3066E cm^{-1}), nitro group vibrations, and C=N stretching (1439C – 1414C cm-1/1448E – 1410E cm-1), while slight discrepancies in C-C bending modes suggest room for improvement (1192C -1137C cm^{-1} /1218E - 1144E cm^{-1}). The comparison across these results highlights the theoretical model's reliability in predicting various vibrational modes. However, it highlights particular areas where potential refinement could improve the accuracy of capturing intricate molecular vibrational frequencies.

C – Shows computational frequency value from DFT.

E – Shows experimental IR absorption value.

3.3.3. Global reactivity descriptors

Chemical reactivity indices, including Chemical hardness (η), Electronegativity (χ), Electron affinity (A), Electronic chemical potential (μ), Electrophilicity index (ω), Ionization potential (I), and Global softness (S), were computed for the synthesized molecules (**4a-4i**) using the B3LYP/TZP model of theory based on the energies of frontier molecular orbitals HOMO and LUMO. According to Koopman's theorem [58–60], the electron affinity (given by $A = -E_{LUMO}$) and ionization potential (given by $I = -E_{HOMO}$) measure

the ability of chemical compounds to donate or accept one electron, respectively. The chemical hardness value represents the stability and reactivity of a chemical system, calculated using $\eta = (E_{LUMO} - E_{HOMO})$ [61]. The global softness (given by $S = 1/\eta$) represents the amount of electron cloud diffused in a molecular system. Moreover, the chemical potential is defined as the negative term of the electronegativity of a molecule [61]. Electrophilicity ($\omega = \mu^2/2\eta$) [62,63] quantifies the capacity of an electrophile to receive electrons from a nucleophile. Vice versa, the electronegativity (given by the equation $\chi = - \mu = -1/2 (E_{LUMO} + E_{HOMO})$) is the ability of a nucleophile to attract electrons from an electrophilic system. The maximal charge acceptance (ΔN_{max}) refers to the maximum amount of charge that a molecular system can accept in a given electronic structure and can be calculated as: $\Delta N_{max} = -(\mu/ \eta)$. In the present study, the computed values are provided in (Table 3). The HOMO and LUMO density distribution on the **4a** compound is illustrated in (Fig. 4), while those of **4b-4i** are given in the supplementary materials.

Briefly, the species are relatively electron-rich, as indicated by their high ionization energy values (varying from 6.2 to 6.6 eV). Thus, these compounds are less likely to lose electrons, potentially contributing to stable interactions with the DNA-Gyrase protein. Despite being electron-rich, they also exhibit a certain degree of electronegativity, suggesting that they can attract electrons and participate in chemical interactions. The high negative chemical potential values highlight the electron-poor nature of these species. They are more likely to act as electrophiles, accepting electrons in reactions. According to Domingo and Pérez, molecules with $\omega > 1.5$ eV have a strong electrophilic character, moderate with $0.8 < \omega < 1.5$ eV, and marginal with $\omega < 0.8$ eV [64]. The results show that all compounds are highly electrophilic, as indicated by higher electrophilic index values (approximately 2.5 eV), and more negative chemical potentials (varying from -4.6 to -4.2 eV), making them more likely to interact with specific amino acid residues or nucleotide bases in DNA-Gyrase.

As listed in (Table 3) and based on Pauling's concept of electronegativity [65], the atoms in compounds **4a**, **4c**, and **4i** ($\chi \approx$ -2.00 eV) have a greater power to attract electrons than **4d**, **4e**, **4f**, **4g**, and **4h** ($\chi \approx$ -1.90 eV). **4b** presents the lowest electronegativity value (-1.77 eV). These compounds with higher

electronegativity may interact with DNA-Gyrase more strongly by forming electrostatic interactions. This electronegative character may also lead to favorable interactions with charged or polar regions of the DNA gyrase protein. The present compounds (**4a**-**4i**) with relatively high hardness values (ranging from 3.5 to 4.0 eV) tend to be resistant to changes in electron density. This property may be advantageous when interacting with proteins like DNA-Gyrase. The rigidity and resistance to conformational changes can be beneficial in forming specific and stable interactions with the protein's binding site. The range of ΔN_{max} values (1.152 to 1.213) highlights the occurrence of intramolecular charge transfer within the compounds, providing insight into their electronic properties and reactivity in various chemical and biological processes. The positive sign of the softness value typically indicates the electron-donating character of these lead compounds. The **4i** compound has the largest absolute affinity value (2,612 eV), making it a better electron acceptor during the interaction with the DNA gyrase protein of the bacterial targets. This aligns well with the antibacterial results.

Table 3: The calculated global reactivity indices and energetic parameters for the synthesized compounds (**4a**-**4i**).

Compound	E_H (eV)	E_L (eV)	I (eV)	A (eV)	χ (eV)	μ (eV)	η (eV)	S (eV^{-1})	ω (eV)	ΔN_{max}
4a	-6,561	-2,548	6,561	2,548	-2,007	-4,555	4,013	0,249	2,585	1,135
4b	-6,057	-2,52	6,057	2,520	-1,769	-4,289	3,537	0,283	2,599	1,213
4c	-6,519	-2,536	6,519	2,536	-1,992	-4,528	3,983	0,251	2,573	1,137
4d	-6,317	-2,516	6,317	2,516	-1,901	-4,417	3,801	0,263	2,567	1,163
4e	-6,375	-2,531	6,375	2,531	-1,922	-4,453	3,844	0,260	2,579	1,159
4f	-6,265	-2,472	6,265	2,472	-1,898	-4,369	3,793	0,264	2,516	1,152
4g	-6,365	-2,514	6,365	2,514	-1,926	-4,439	3,851	0,259	2,559	1,153
4h	-6,301	-2,480	6,301	2,480	-1,911	-4,391	3,821	0,262	2,522	1,149
4i	-6,659	-2,612	6,659	2,612	-2,024	-4,636	4,047	0,247	2,655	1,146

3.3.4. Molecular Electrostatic Potential (MEP) analysis

The MEP surfaces were calculated for all the optimized structures, defined as the isosurfaces of ρ = 0.03. These surfaces are useful for analyzing the charge distribution across the molecules. Various

colors illustrate the diverse range of electrostatic potential values; deep-red regions signify areas rich in electrons, indicative of nucleophilic character, whereas deep-blue regions indicate areas with relatively lower electron density, suggesting electrophilic character. Between these two regions is the neutral one (in green) [45,66–68]. In the results, the deep-red is centered on the oxygen atoms, especially on the oxygen of -NO_2 groups, representing the highest nucleophilic character in these compounds (high electronegativity). Meanwhile, the hydrogen atom from the alcoholic function (-OH) is the most acidic region (in deep blue). The oxygens of the methoxy (-OCH_3) groups are less nucleophilic. The carbon atoms from the aromatic system (quinoline) represent the neutral region in the compounds **4c**, **4d**, **4f**, and **4h**. This is explained by the donor effect of the methyl (-CH_3) groups, which are almost situated on the opposite side of the -NO_2 group. This gives the green color to these parts of the mentioned compounds. The same part is colored yellow, representing a weak nucleophilic character. Compound **4i**, positioned symmetrically with methoxy groups, is colored neither deep green nor deep yellow, displaying an intermediary color. This is due to the methoxy groups' symmetrical placement, leading to a modest reduction in its weak nucleophilic nature, bringing it closer to a neutral state. Note that the hydrogen atoms from the -CH_3 groups are more electrophilic than the hydrogen from the conjugated quinoline system. In conclusion, the addition of -CH_3 groups to the quinoline system brings us closer to the neutral region by increasing their nucleophilic character. The results of the electrostatic potential maps are shown in (Fig. 4).

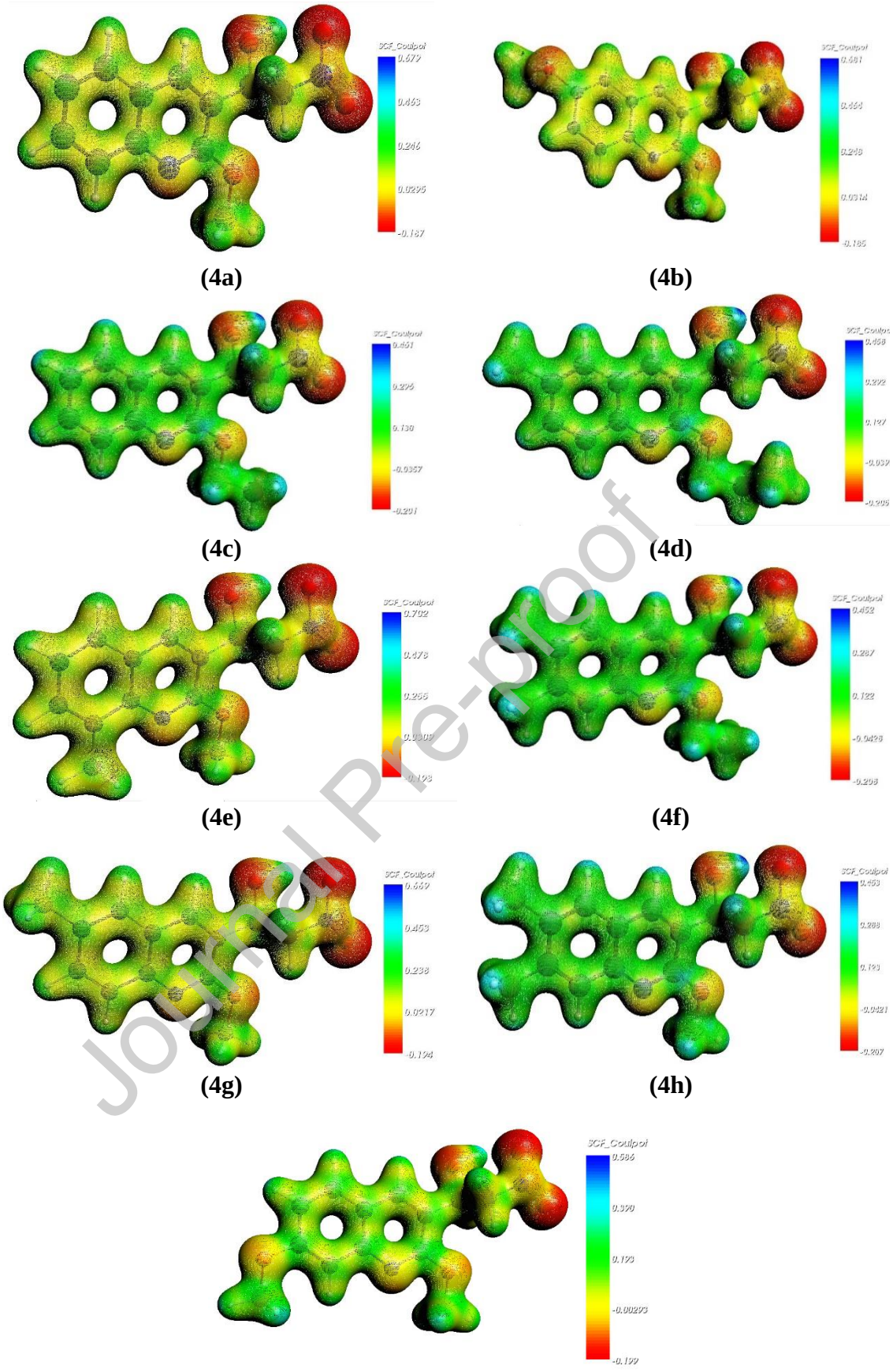

Fig. 4. Molecular Electrostatic Potential Surfaces of (**4a-4i**) compounds (ρ = 0.03).

3.3.5. Topological QTAIM analysis

The quantum theory of atoms in molecules (QTAIM) approach was employed to examine the character of the interactions within the studied structures. Different types of interactions are classified in the literature; closed-shell interactions are characterized by a small electron density at the bond critical point (ρ_{BCP}) and a positive Laplacian value ($\nabla^2\rho_{BCP}$), such as Hydrogen Bonds, van der Waals, or ionic interactions [69]. In contrast, open-shell interactions, known as covalent interactions, have a large electron density at the bond critical point (ρ_{BCP}), and their Laplacian ($\nabla^2\rho_{BCP}$) is negative. Following the methodology introduced by Rozas et al. [70], the nature of interaction can be categorized based on the HBCP and the Laplacian of the electron density at the BCP ($\nabla^2\rho_{BCP}$). The degree of covalency of a given interaction is reflected by the magnitude of H_{BCP}. The covalent character is defined by $\nabla^2\rho_{BCP} < 0$ and $H_{BCP} < 0$, representing strong interactions. Partially covalent character is denoted by $\nabla^2\rho_{BCP} > 0$ and HBCP < 0, indicating medium strength, while the electrostatic character is given by $\nabla^2\rho_{BCP} > 0$ and HBCP > 0, mainly representing weak interactions. In our study, we have only considered additional intramolecular atomic interactions. QTAIM / B3LYP / TZP calculations indicate that a specific pattern of O–H···O=N interactions is observed in all the structures. Analyzing the provided data (listed in the supplementary information) reveals that the density values for the selected BCPs are uniformly below 0.1. These values, coupled with the Laplacian values ($\nabla^2\rho$) being relatively small and positive, indicate a closed-shell interaction, predominantly characterized as non-covalent in nature [44,71]. The (3, -1) BCPs associated with these bonds have negative values of the total electron energy density ($H_{BCP} < 0$), defining their partially covalent character. It is noteworthy that another intramolecular interaction is obtained for the **4d** structure. This critical point has a relatively small positive value of ρ_{BCP}, positive values of the Laplacian, and $H_{BCP} > 0$, guaranteeing the existence of weak H-bonding, which indicates that the C–H···O=N interaction has a significant electrostatic nature. According to Bader et al., the π-component at the bond critical points is defined by the ellipticity (ε) values. The π-component is high in the **4d** structure at the

rest of RCP (ε = 20.430) and RCP (ε = 4.840), indicating very high recovery between the concerned atoms. The π-component is greater in all the structures at the RCPs ($0.270 \leq \varepsilon \leq 0.330$), indicating, in turn, high recovery between the concerned atoms. The low value of ellipticity at the selected BCP indicates that this bond has negligible π-character ($0.03 \leq \varepsilon \leq 0.05$), suggesting an absence of conjugation between the concerned atoms. (Fig. 5) presents molecular plots for all the studied structures examined in this work. The Bond critical points (BCPs) are illustrated in red, and the Ring critical points (RCPs) are in green.

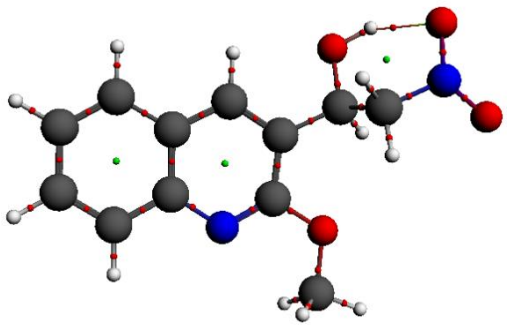

(4a)

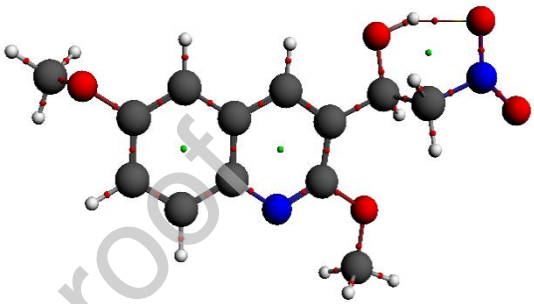

(4b)

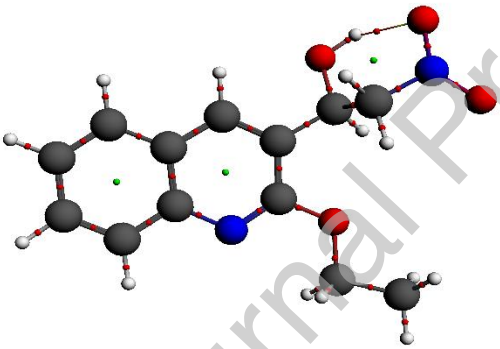

(4c)

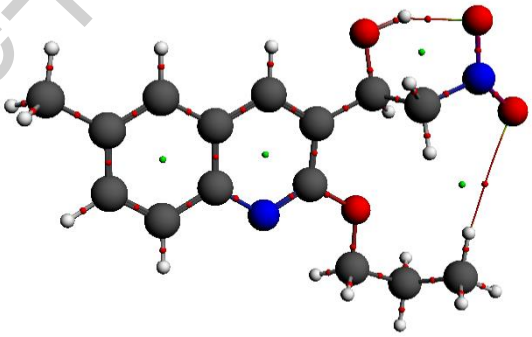

(4d)

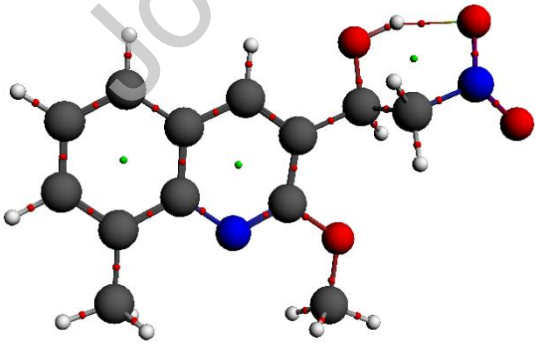

(4e)

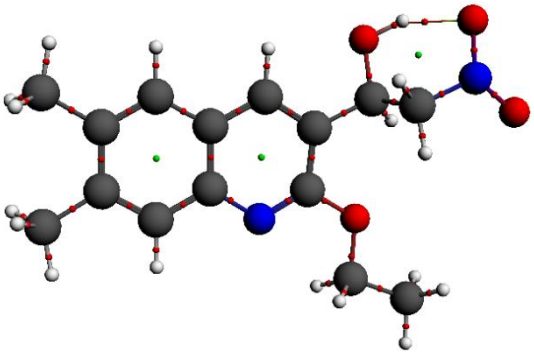

(4f)

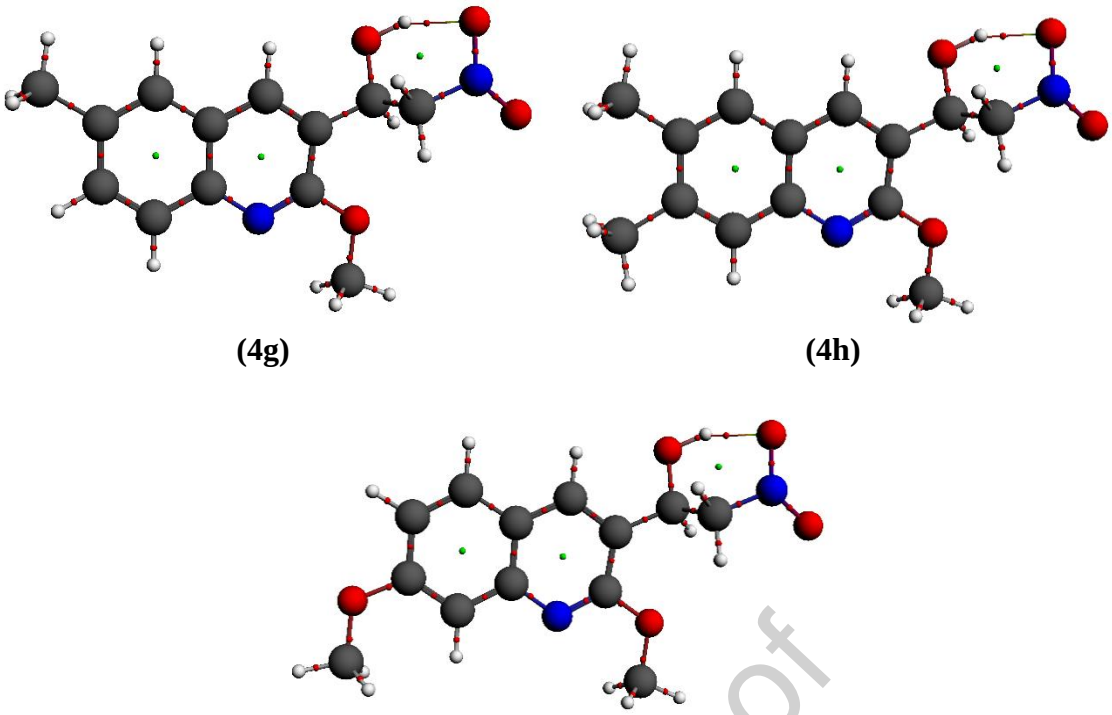

(4g) **(4h)**

(4i)

Fig. 5. QTAIM analysis shows the inter and intramolecular interactions Bond critical points (BCPs, red), and Ring critical points (RCPs, green) of (**4a-4i**) compounds.

3.4. Molecular Docking Analysis

Molecular docking can serve as a valuable tool for modeling the antimicrobial activity of potential drug molecules, including those targeting DNA proteins.

DNA gyrase is a pivotal enzyme that regulates DNA topology in bacteria, playing a crucial role in processes such as DNA replication, transcription, and repair [72,73]. Specifically, it introduces negative supercoiling into the DNA double helix, a process essential for various cellular functions. This enzyme acts by breaking and resealing one strand of the DNA, facilitating DNA unwinding during replication or transcription. DNA gyrase is particularly vital in bacteria as it helps alleviate torsional strain ahead of the replication fork or transcription bubble, ensuring the smooth progression of these processes. As a type II topoisomerase, DNA gyrase differs from other topoisomerases by introducing negative supercoils into DNA, making it a unique and essential target for certain antibiotics like fluoroquinolones, for instance, Ciprofloxacin. Inhibition of DNA gyrase by these antibiotics disrupts bacterial DNA replication,

ultimately leading to bacterial cell death. Understanding the structure and function of DNA gyrase is critical for developing antibacterial agents and studying bacterial physiology. It remains a focus of research in the field of microbiology and drug discovery due to its vital role in bacterial DNA metabolism. (Table 4) provides a detailed overview of molecular docking results for nine synthesized ligands (**4a-4i**) within the active cavity of DNA-gyrase (PDB Code: 1ZNK). Affinity values, types of interactions, residual amino acids, and interaction lengths are presented for each ligand. The results are also compared with those of the standard drug (Ciprofloxacin) and the co-crystallized ligand (Clorobiocin). Hydrogen bonds play a pivotal role in ligand-receptor interactions, contributing significantly to binding stability and specificity (Fig. 6).

Table 4: Molecular docking results of synthesized (**4a-4i**) compounds against DNA gyrase (PDB ID 1KZN).

		Residual amino-acid interactions	
Ligand	**Affinity (Kcal/ mol)**	**Conventional H-Bonds/ Carbon H-Bond (Donor-Acceptor)**	**Hydrophobic/Pi-cation/Pi-anion/ Pi-sigma/Pi alkyl and van der Waals interactions**
4a	-7.3	A:ASN46	A:THR165, A:ILE78, A:ILE90, A:VAL120, A:VAL43, A:ALA47, A:VAL167.
4b	-6.8	A:ASN46, A:ARG76, A:PRO79, A:ASP73, A:THR165	A:ASN46, A:ILE78, A:THR165, A:ALA47, A:VAL71
4c	-7.1	A:ASN46, A:GLY77, A:THR165	A:THR165, A:ILE90, A:VAL43 , A:ALA47, A:VAL167, A:ILE78
4d	-7.4	A:GLY77	A:ASN46, A:ILE78, A:THR165, A:ALA47, A:VAL71, A:ILE90
4e	-7.2	A:GLY77, A:ASN46	A:THR165, A:ILE78, A:ILE90, A:VAL120, A:ALA47
4f	-7.4	A:ASN46, A:ARG76	A:ILE78
4g	-7.0	/	A:ILE78, A:THR165, A:ALA47, A:VAL71, A:ILE90, A:MET91, A:VAL120, A:VAL167
4h	-7.4	A:ASN46, A:ARG76, A:GLU50	A:ILE78, A:ILE90
4i	-6.3	A:ASN46, A:ARG76, A:VAL71	A:VAL43, A:VAL167, A:ILE90, A:ALA47, A:ILE78
Ciprofloxacin (CFX)	-7.3	A:ARG76, A:ARG136, A:THR165, A:ASN46	A:ASP73, A:GLU50, A:ILE90, A:PRO79, A:ILE78

Clorobiocin (CBN)	-9.1	A:ARG136, A:ASN46, A:ASP73	A:ARG76, A:GLU50, A:THR165, A:ASN46, A:ALA86, A:VAL71 A:ALA47, A:PRO79

Where: CBN = Clorobiocin, CFX= Ciprofloxacin.

The molecular docking results reveal distinctive binding profiles for ligands **4a** to **4i** within the active cavity of DNA-gyrase, shedding light on their specific interaction patterns. Ligand **4a** forms a conventional hydrogen bond with A:ASN46, aligning coherently with the established binding patterns of Ciprofloxacin and Clorobiocin. The distinctive versatility of **4a** is prominently elucidated through pi-sigma interactions with A:THR165 and alkyl interactions involving A:ILE78, A:ILE90, and A:VAL120. This diversified interaction repertoire mirrors Clorobiocin's proficiency in forming multiple hydrogen bonds and engaging in diverse pi interactions. Ligand **4b** manifests a binding profile reminiscent of Clorobiocin, characterized by conventional hydrogen bonds with A:ASN46 and A:ARG76. The presence of carbon-hydrogen bonds with A:PRO79 and A:ASP73 signifies an affinity for both hydrogen bond donor and acceptor sites, aligning with the diverse hydrogen bond interactions observed for Ciprofloxacin. For ligand **4c**, the occurrence of conventional hydrogen bonds with A:ASN46 and A:GLY77, coupled with pi-sigma and pi-alkyl interactions, resonates with the intricate hydrogen bond interactions and diverse pi interactions observed for both Ciprofloxacin and Clorobiocin. Ligand **4d**'s flexibility, evident in the formation of conventional hydrogen bonds and diverse alkyl interactions, aligns seamlessly with Clorobiocin's versatile binding profile, which includes conventional hydrogen bonds, pi-cation interactions, and pi-sigma interactions. The binding profile of ligand **4e**, characterized by conventional hydrogen bonds, pi-sigma interactions, and alkyl interactions, mirrors the diverse interactions observed for both Ciprofloxacin and Clorobiocin. Ligand **4f** shares similarities with Clorobiocin in forming conventional hydrogen bonds and pi-alkyl interactions with aromatic amino acids, emphasizing its engagement with aromatic residues within the active site. Ligand **4g** primarily engages in pi-sigma interactions, akin to Ciprofloxacin's pi-sigma interactions with A:ILE78, indicating a specific affinity for aromatic amino acids. Concurrent alkyl interactions further contribute to its binding strength, reminiscent

of Clorobiocin's alkyl interactions with various residues. In contrast, ligand **4h** distinguishes itself by forming conventional hydrogen bonds with (A:ASN46, A:ARG76), a Carbon-Hydrogen Bond with (A:GLU50), alkyl interactions with (A:ILE78, A:ILE90), and pi-alkyl interactions with (A:ILE78).

The simultaneous demonstration of hydrogen bond donor and acceptor capabilities aligns with Ciprofloxacin's interactions, while the inclusion of pi-sigma interactions adds a unique facet to its binding profile. Finally, ligand **4i** shares similarities with Clorobiocin in forming conventional hydrogen bonds and carbon-hydrogen bonds. Alkyl interactions and pi-alkyl interactions further underscore its hydrophobic interactions within the active site, reflecting the diverse interactions observed for both reference compounds.

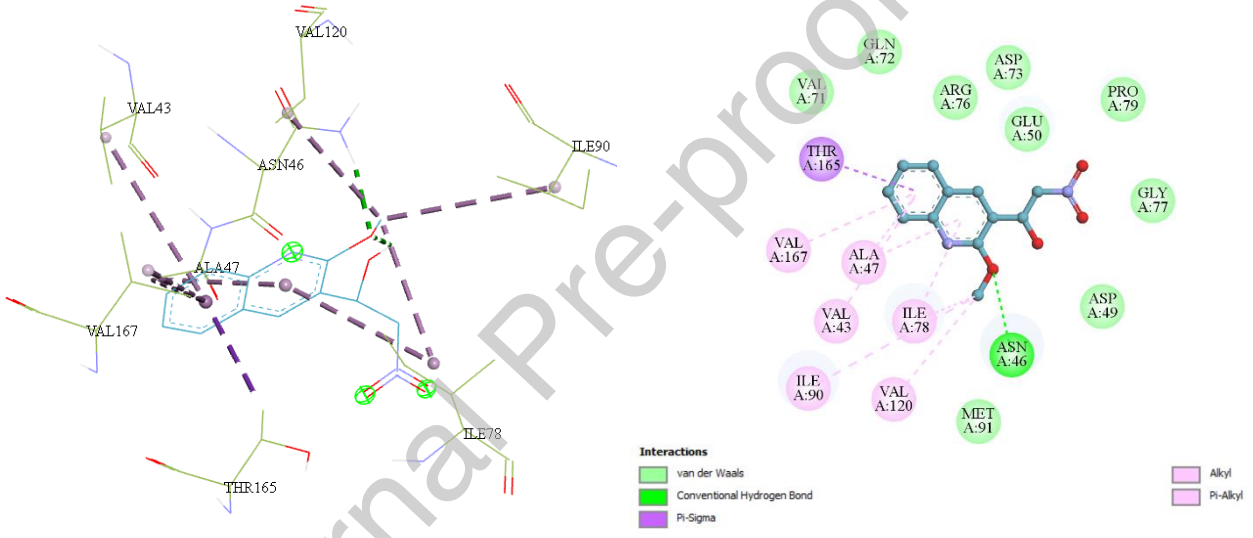

(4a)

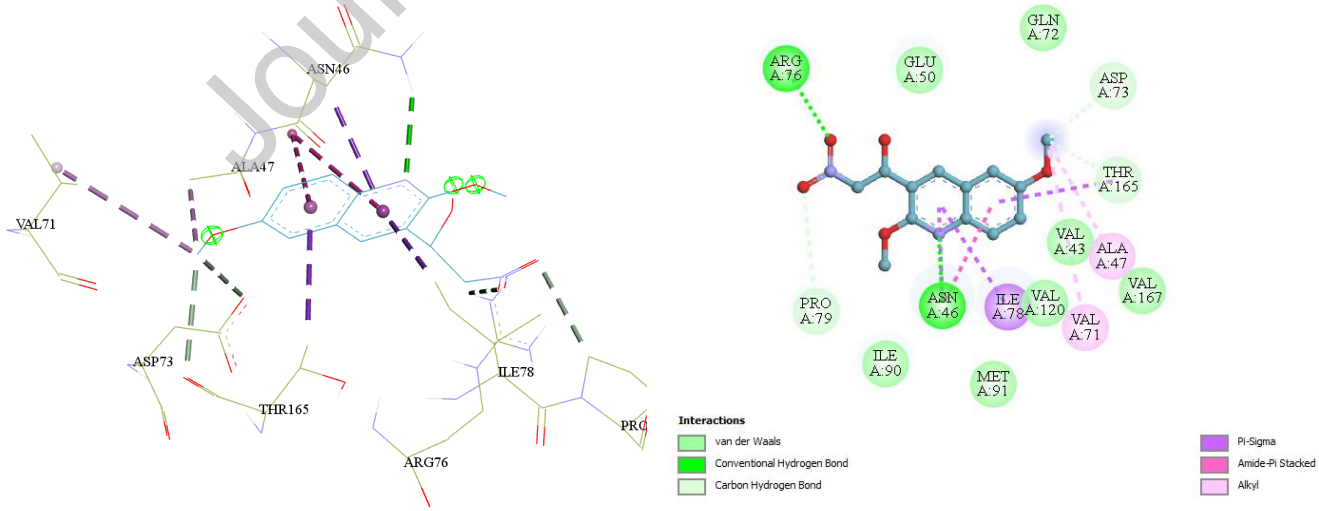

(4b)

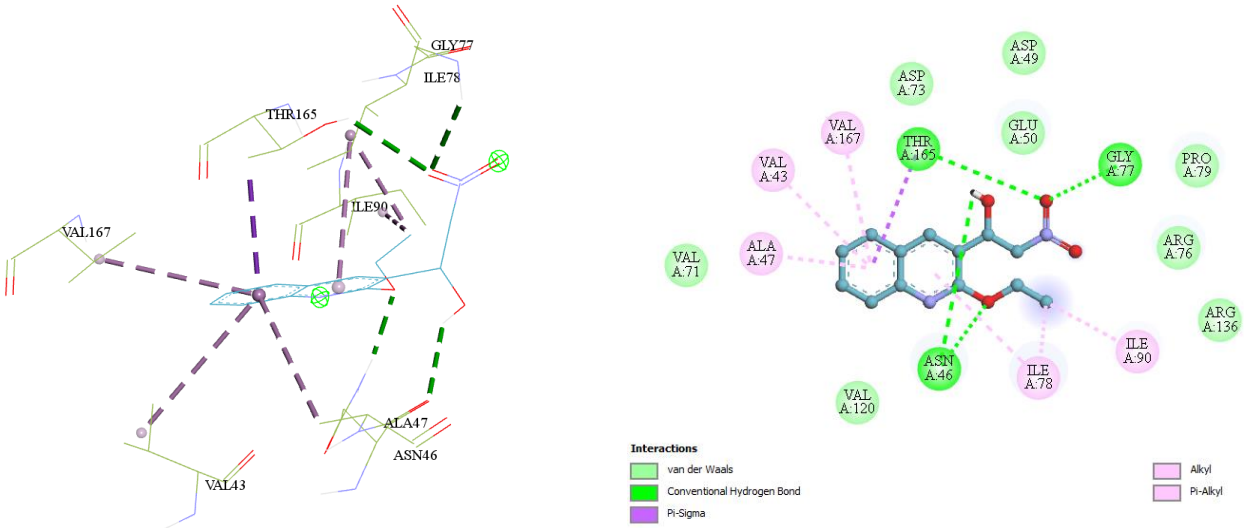

(4c)

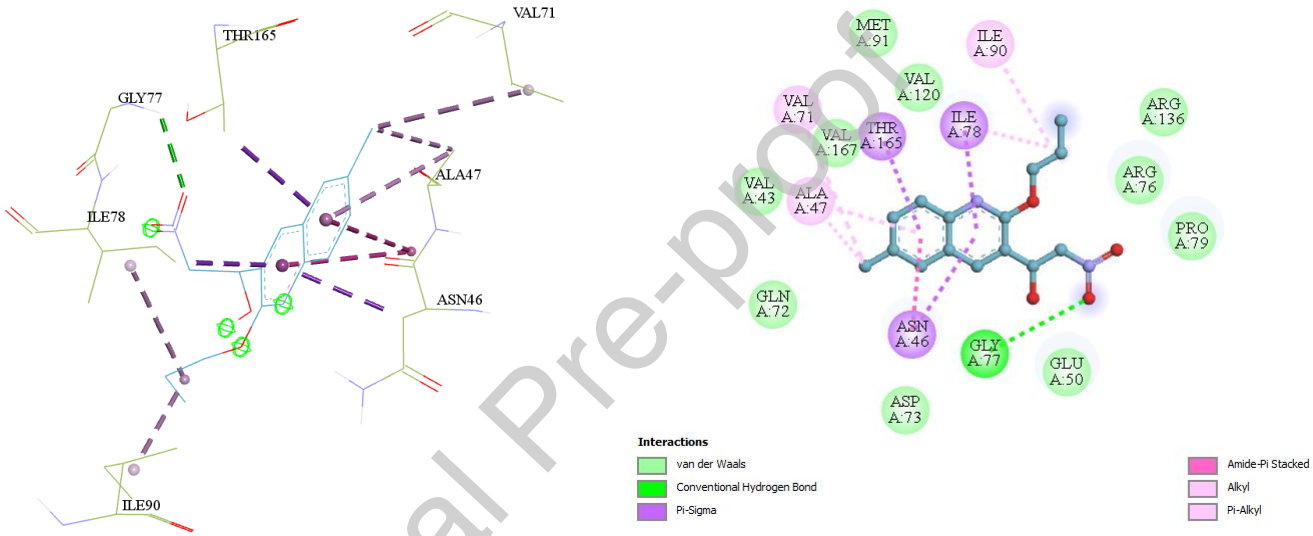

(4d)

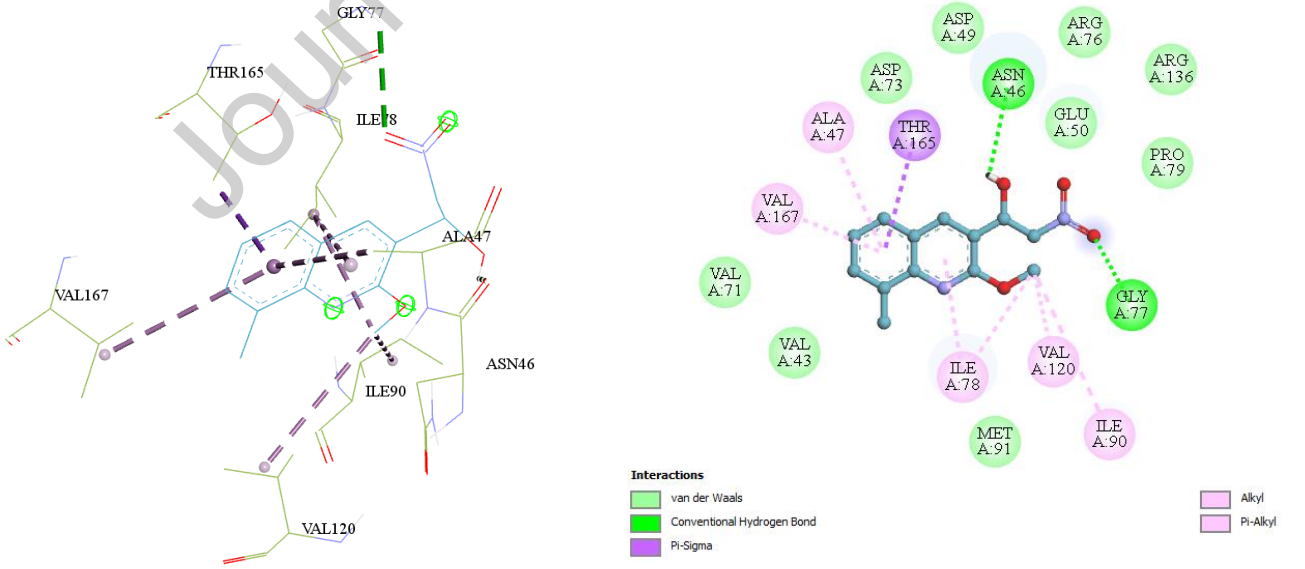

(4e)

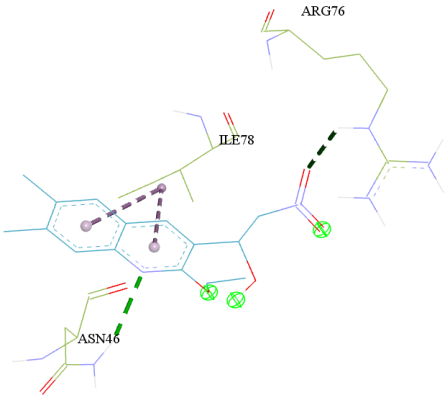

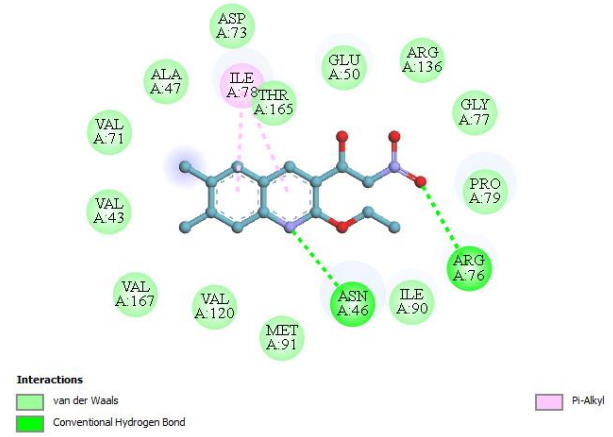

(4f)

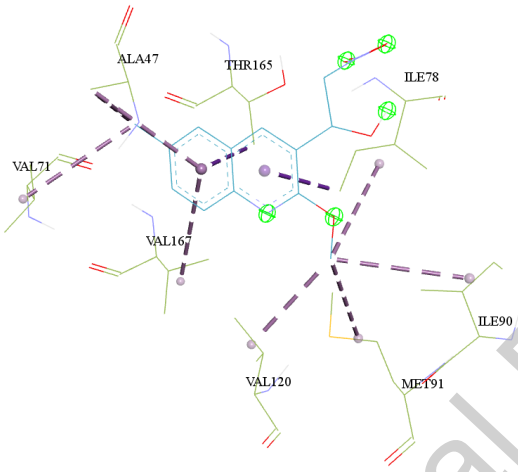

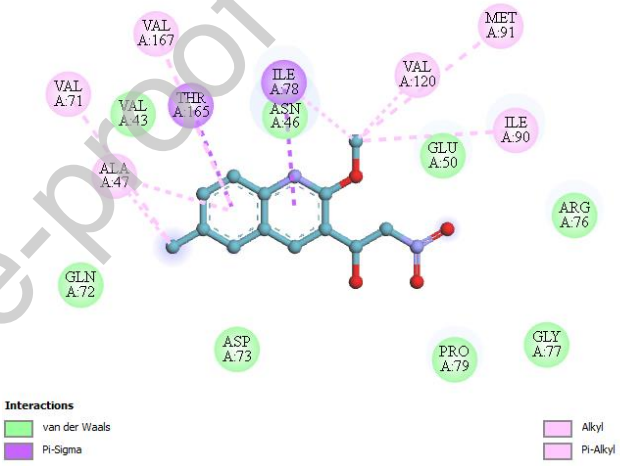

(4g)

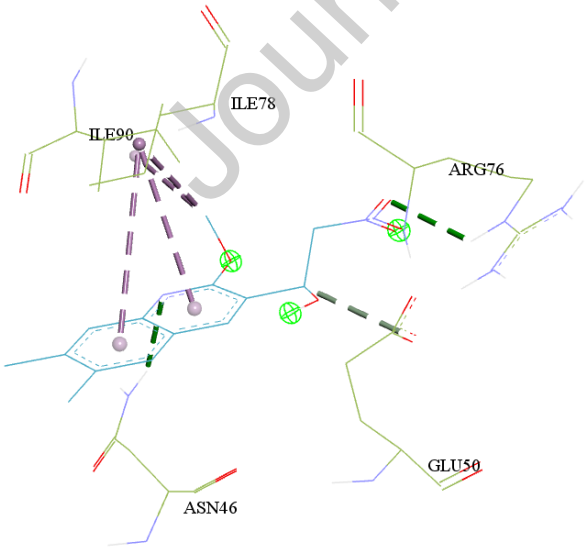

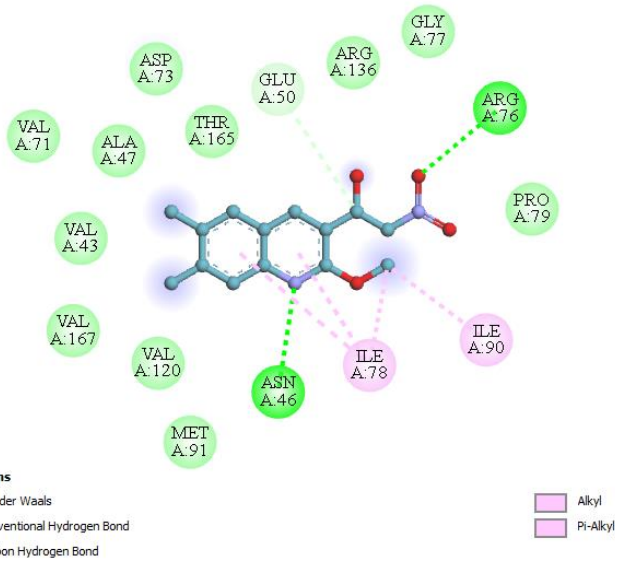

(4h)

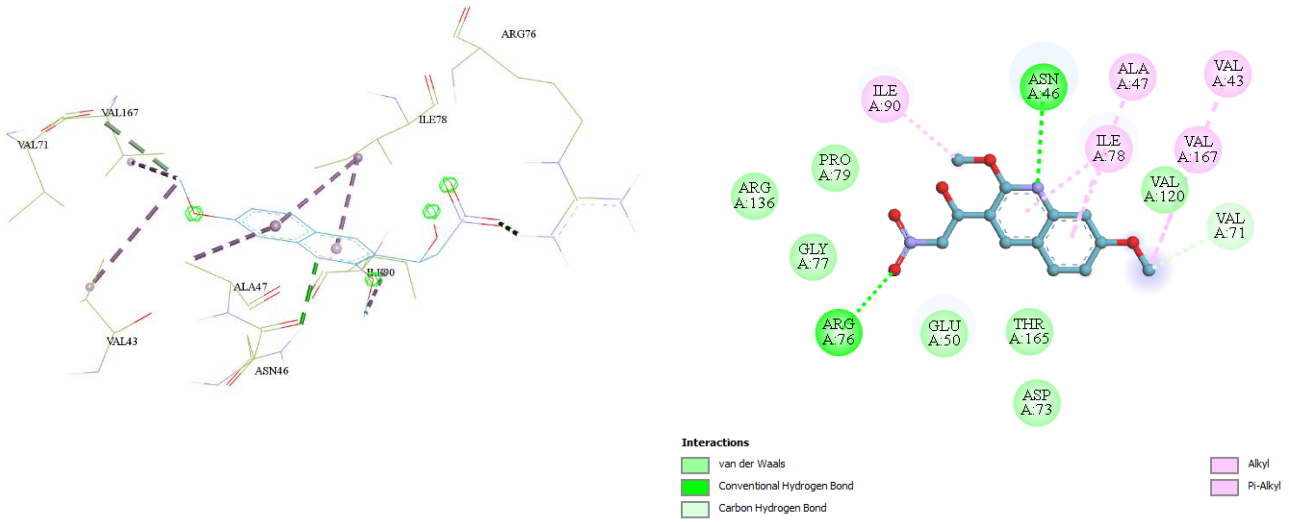

(4i)

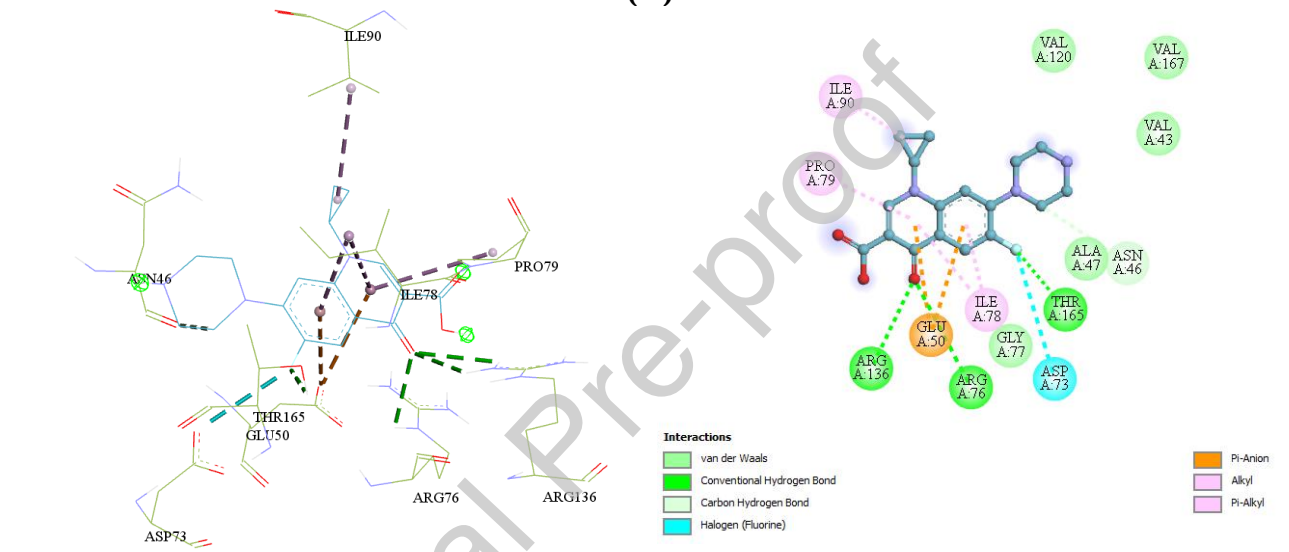

Ciprofloxacin

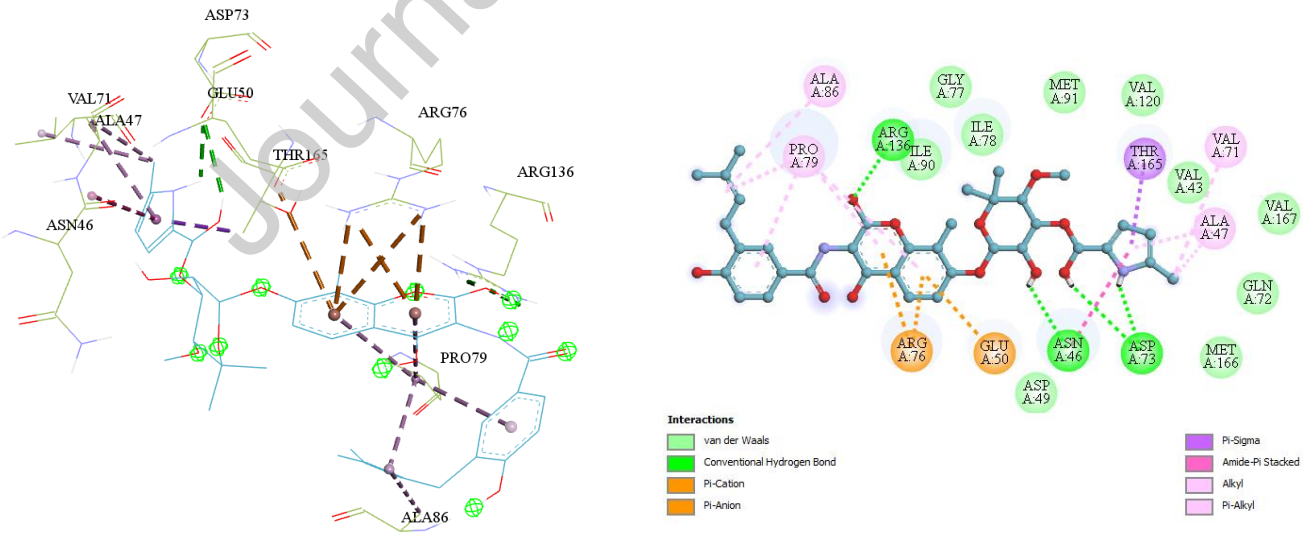

Clorobiocin

Fig. 6. 2D and 3D molecular docking of lead compounds (**4a-4i**), standard drug (Ciprofloxacin), and co-crystallized ligand (Clorobiocin) into the active cavity of DNA gyrase (PDB ID 1KZN).

For the re-docking validation step, the RMSD value of the co-crystallized ligand (Clorobiocin) was found to be excellent at 0.454 Å, and a docking score of -9.1 kcal/mole, as depicted in (Fig. 7) (Reference molecule (in red) and re-docked ligand (in blue)).

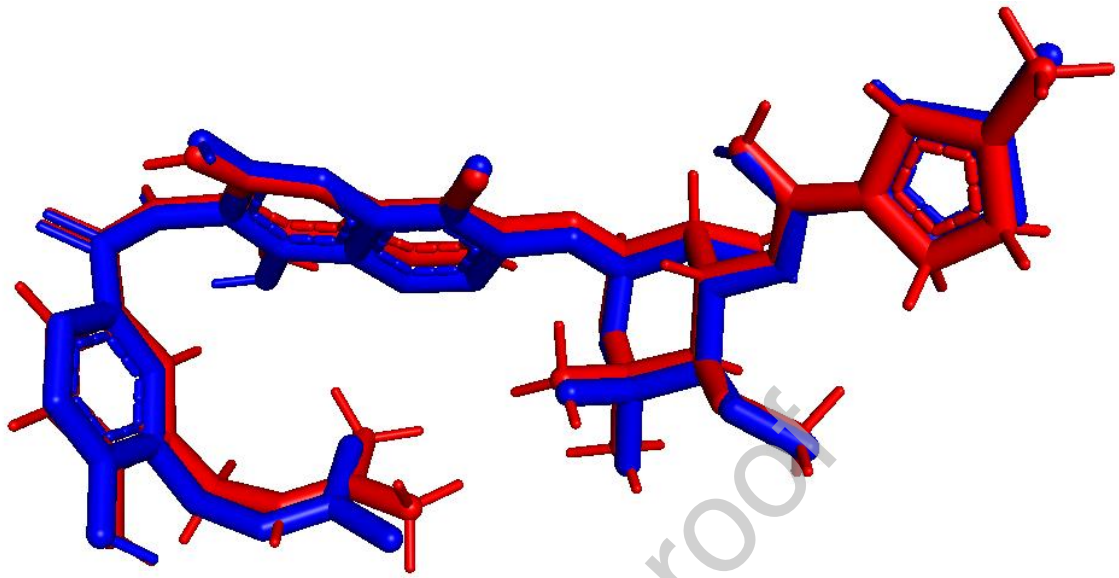

Fig. 7. Validation step of Clorobiocin

3.5. *In silico,* Physicochemical properties, pharmacokinetics, and drug-likeness profile

Prediction of ADME parameters, physicochemical descriptors, pharmacokinetic properties, drug-like properties, and medicinal chemistry friendliness of synthesized compounds was conducted using the SwissADME online server (http://www.swissadme.ch/). The results of the SwissADME analysis are presented in (Table 5), showcasing the principal physicochemical parameters.

Table 5: Physicochemical parameters of the nine compounds (**4a-4i**).

	Physiochemical properties, lipophilicity and water solubility							
	TPSA (Å²)	**ABS (%)**	**MW (g/mol)**	**HBA**	**HBD**	**nrotb**	**Log P (iLOGP)**	**Log S (ESOL)/ Log S (Ali)/ Log S (SILICOS-IT)**
4a	88.17	78.58	248.23	5	1	4	1.24	-2.43/-2.90/-3.57
4b	97.40	75.39	278.26	6	1	5	1.81	-2.49/-3.06/-3.69
4c	88.17	78.58	262.26	5	1	5	1.66	-2.67/-3.28/-3.97
4d	88.17	78.58	290.31	5	1	6	2.46	-3.30/-4.20/-4.76
4e	88.17	78.58	262.26	5	1	4	1.95	-2.73/-3.28/-3.96
4f	88.17	78.58	290.31	5	1	5	2.42	-3.26/-4.04/-4.74

4g	88.17	78.58	262.26	5	1	4	1.74	-2.73/-3.28/-3.96
4h	88.17	78.58	276.29	5	1	4	1.09	-3.03/-3.65/-4.34
4i	97.40	75.39	278.26	6	1	5	1.98	-2.49/-3.06/-3.69

According to the predicted results, all compounds (**4a**–**4i**) qualify as orally active drugs as they adhere to "Lipinski's rule of five" criteria (lipophilicity (LogP) < 5, HBD ≤ 5, HBA ≤ 10, molecular weight (g/mol) ≤ 500 g/mol, polarity: 20 Å ≤ TPSA (Å2) ≤ 140 Å, and flexibility (rotatable bonds): < 9) [74]. Additionally, these compounds exhibit good water solubility (aqueous), with values predicted using three methods: logS (ESOL, ALI, and SILICOS-IT) [75]. Moreover, they pass various additional filters, including Lipinski's [74] and Veber's rules [76], as well as Ghose filters [77], Egan [78], and Muegge [79] (Table 6). The compounds also demonstrate bioavailability scores of approximately 0.55, indicating their specificity (with no warnings for pan assay interference compounds (PAINs)). These factors collectively suggest the oral bioavailability of the studied compounds. The percentage of oral absorption (%ABS) was measured using the following equation [77]:

$$\%ABS = 109 - 0.345\ TPSA$$

The predicted results showed that the corresponding oral absorption percentage ranged from 75.39% to 78.58%, indicating high permeability, absorption, and effective transport through a biological membrane. Compound **4a** complies with drug-likeness parameters; it is highly soluble but exhibits one violation in medicinal chemistry (Lead-likeness) due to a high molecular weight (MW < 250). The drug-likeness assessment of the bioactive compounds listed in (Table 6), along with their various parameters, is depicted using the SwissADME bioavailability radar in (Fig. 8).

Table 6: Some predicted drug-likeness and medicinal chemistry parameters of the compounds (**4a-4i**).

Drug-likeness and Medicinal Chemistry								
	Ghose	**Veber**	**Egan**	**Muegge**	**Lipinski, violation**	**Bioavailability Score**	**Pains (No Alert)**	**Lead-likeness**
4a	Yes	Yes	Yes	Yes	Yes, 0	0.55	0	No (1 violation: MW<250)
4g	Yes	Yes	Yes	Yes	Yes, 0	0.55	0	Yes
4e	Yes	Yes	Yes	Yes	Yes, 0	0.55	0	Yes
4b	Yes	Yes	Yes	Yes	Yes, 0	0.55	0	Yes
4i	Yes	Yes	Yes	Yes	Yes, 0	0.55	0	Yes
4h	Yes	Yes	Yes	Yes	Yes, 0	0.55	0	Yes
4c	Yes	Yes	Yes	Yes	Yes, 0	0.55	0	Yes
4f	Yes	Yes	Yes	Yes	Yes, 0	0.55	0	Yes
4d	Yes	Yes	Yes	Yes	Yes, 0	0.55	0	Yes

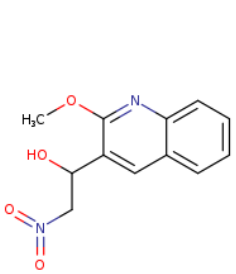

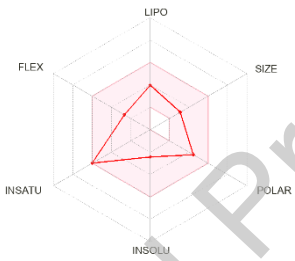

(4a)

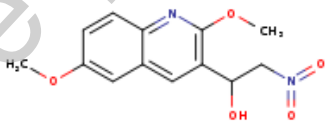

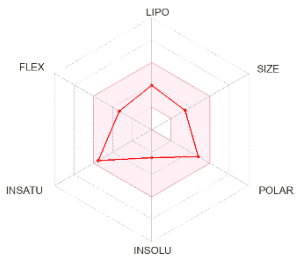

(4b)

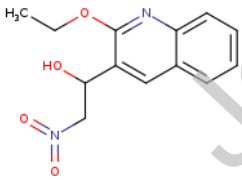

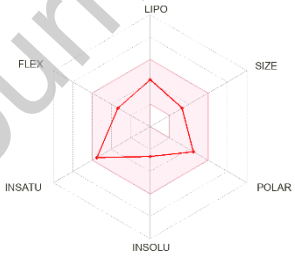

(4c)

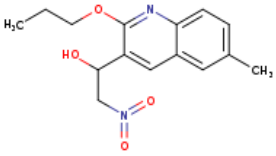

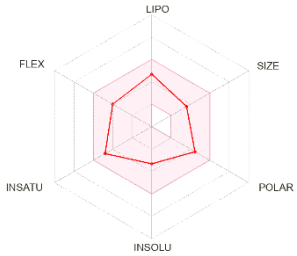

(4d)

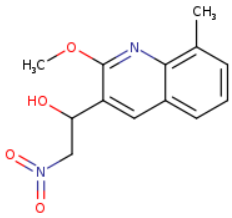

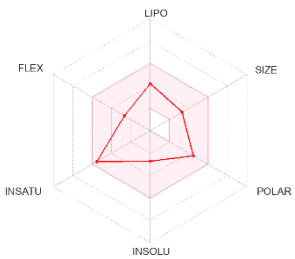

(4e)

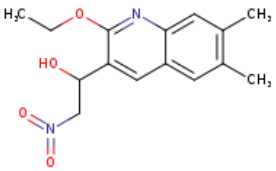

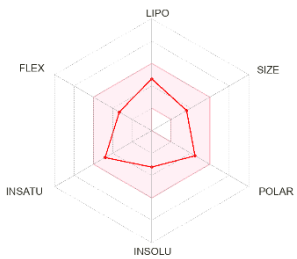

(4f)

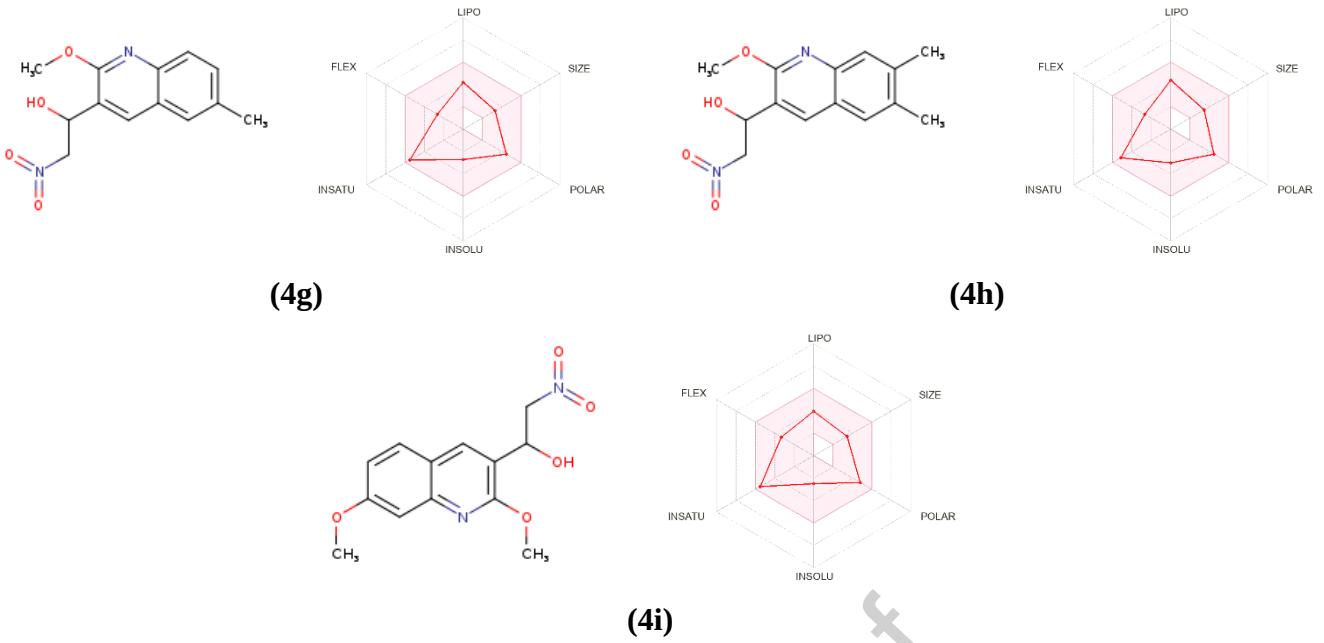

Fig. 8. The SwissADME bioavailability radar displays various bioactive drug-like molecules, with each property (flexibility, lipophilicity, molecular weight, and solubility) represented by pink regions.

Furthermore, the table below (Table 7) provides an overview of specific pharmacokinetic parameters investigated computationally through the *in silico* SwissADME web server. These parameters include Gastrointestinal absorption, Blood-brain barrier permeability, Substance interacting with P-glycoprotein, Inhibitor affecting cytochrome P450 1A2, Inhibitor affecting cytochrome P450 2C19, Inhibitor affecting cytochrome P450 2C9, Inhibitor affecting cytochrome P450 2D6, and Inhibitor affecting cytochrome P450 3A4, abbreviated as GIA, BBB, P-gp substrate, CYP1A2 inhibitor, CYP2C19 inhibitor, CYP2C9 inhibitor, CYP2D6 inhibitor, and CYP3A4 inhibitor, respectively.

Table 7: Some pharmacokinetics parameters obtained at the level of SwissADME web server.

	Pharmacokinetics								
	GIA	**BBB permeant**	**P-gp substrate**	**CYP1A2 inhibitor**	**CYP2C19 inhibitor**	**CYP2C9 inhibitor**	**CYP2D6 inhibitor**	**CYP3A4 inhibitor**	**Log Kp (skin Permeation (cm/s))**
4a	High	No	No	No	No	No	No	No	-6.79

4b	High	No	No	**Yes**	No	No	No	No	-7.00
4c	High	No	No	No	**Yes**	No	No	No	-6.61
4d	High	No	No	**Yes**	**Yes**	No	No	No	-6.15
4e	High	No	No	No	No	No	No	No	-6.61
4f	High	No	No	**Yes**	**Yes**	No	No	No	-6.27
4g	High	No	No	No	No	No	No	No	-6.61
4h	High	No	No	No	No	No	No	No	-6.44
4i	High	No	No	**Yes**	No	No	No	No	-7.00

The tested compounds were well absorbed by the gastrointestinal system and exhibited medium skin penetration with Log Kp values ranging from -6.15 to -7.00. These compounds do not exhibit inhibitory effects on the CYP2D6 enzyme, suggesting they are unlikely to engage in interactions with either CYP2D6 inhibitors or inducers. Theoretically, all the studied compounds are not inhibitors of the mentioned enzymes, except for **4c**, **4f**, and **4d**, which are useful as CYP2C19 enzyme inhibitors, and **4b**, **4i**, **4f**, and **4d** as CYP1A2 enzyme inhibitors.

4. Conclusion

In this study, we outlined a simple and efficient method for synthesizing new β-nitroaldol quinoline derivatives (4a-4i) using the Henry reaction. The resultant compounds were successfully obtained, indicating favorable yields. Structures of all synthesized compounds were confirmed by usual spectroscopic techniques. The synthesized compounds exhibited moderate antifungal properties against *Candida albicans* and effective antibacterial effects on both *vancomycin-resistant E. faecium* and *Staphylococcus aureus* strains. The compound 4e is the most active molecule, displaying a Minimum Inhibitory Concentration (MIC) of 25 µg/mL. However, none of the compounds showed activity against Gram-negative bacterial strains. The results reveal notable relationships in activity, specifically indicating a decrease in antimicrobial activity with each increase in the alkoxyl carbon chain at position 2. A high level of consistency was evident between the DFT study and experimental results. The lead molecules exhibit notable chemical reactivity, these findings support their inhibition ability against the 1KZN protein. These attributes suggest the potential for substantial biological activities. Molecular electrostatic potential (MEP) analysis disclosed distinct reactivity patterns due to the presence of various reactive

functional groups. Notably, the -NO_2 group exhibited a strong nucleophilic character, while the hydrogen atoms from -CH_3 groups and the alcoholic (-OH) functional group displayed electrophilic tendencies. Insights from Quantum Theory of Atoms in Molecules (QTAIM) results indicated the formation of hydrogen bonds between the alcoholic hydrogen and -NO_2 groups. Additionally, a weaker hydrogen bond involving the hydrogen atom of methyl group from the propyl moiety was identified, supported by a high π-component contribution highlighted by the ellipticity value (ε = 20.430), signifying substantial interaction between the respective atoms. Moreover, molecular docking simulations elucidate the antimicrobial potential of synthesized ligands targeting DNA gyrase, providing insights into diverse interactions. Thus, molecular docking of ligands **4a** to **4i** in the DNA-gyrase active cavity reveals diverse binding profiles, including conventional hydrogen bonds and unique pi-interactions. Ligand **4a** exhibits versatile binding akin to Clorobiocin, forming hydrogen bonds and engaging in pi-sigma interactions. Ligands **4b** to **4i** display specific interactions mirroring established patterns of reference compounds. Comparative analysis with standard drugs (Ciprofloxacin and Clorobiocin) and the re-docking validation affirms accuracy of the molecular docking results, with an RMSD of 0.454 Å and a docking score of -9.1 kcal/mole, this creating a bridge between computational predictions and experimental antimicrobial effects. Finally, *in silico* predictions using the SwissADME online server affirm the compounds' adherence to Lipinski's rule of five, suggesting potential as orally active drugs with favorable pharmacokinetic properties. The link between computational analysis and drug-likeness parameters, as seen in compound **4a** with one violation in medicinal chemistry (Lead-likeness) due to its elevated molecular weight (MW<250), establishes a connection between molecular design and potential oral bioavailability. These interconnected analyses provide a comprehensive and cohesive understanding of the synthesized nitroaldol quinoline derivatives, linking their structural features to biological activities, electronic properties, vibrational characteristics, and potential pharmacokinetic profiles. The study contributes valuable insights into the development of potential antimicrobial agents, creating a bridge between synthesis, biological effects, and computational predictions.

Author Contributions

FG conceived and designed the study, conducted the experimental synthesis and structural analysis, and led the research efforts; OK was responsible for the theoretical investigation, played a role in conceptualizing the study, and contributed to drafting and revising the manuscript; ZC conducted the experimental biological investigation; LL drafted the biological section of the manuscript; WB carried out the mass spectroscopy analysis, NB participated in the investigation, and contributed to manuscript revisions; ML drafted the manuscript; PM performed the NMR structural analysis; All authors read and approved the final manuscript submission.

Conflicts of interest

There are no conflicts to declare.

Acknowledgments

The authors wish gratefully to express thanks to the Scientific and Technical Research Centre in Physico-Chemical Analyses CRAPC, Bou-Ismail, Tipaza, Algeria. FG thanks Yacine Laichi for data collection and Spectral FTIR, ^{1}H NMR, and ^{13}C NMR analyses.

References

[1] E.A. Ashley, M. Dhorda, R.M. Fairhurst, C. Amaratunga, P. Lim, S. Suon, S. Sreng, J.M. Anderson, S. Mao, B. Sam, C. Sopha, C.M. Chuor, C. Nguon, S. Sovannaroth, S. Pukrittayakamee, P. Jittamala, K. Chotivanich, K. Chutasmit, C. Suchatsoonthorn, R. Runcharoen, T.T. Hien, N.T. Thuy-Nhien, N.V. Thanh, N.H. Phu, Y. Htut, K.-T. Han, K.H. Aye, O.A. Mokuolu, R.R. Olaosebikan, O.O. Folaranmi, M. Mayxay, M. Khanthavong, B. Hongvanthong, P.N. Newton, M.A. Onyamboko, C.I. Fanello, A.K. Tshefu, N. Mishra, N. Valecha, A.P. Phyo, F. Nosten, P. Yi, R.

Tripura, S. Borrmann, M. Bashraheil, J. Peshu, M.A. Faiz, A. Ghose, M.A. Hossain, R. Samad, M.R. Rahman, M.M. Hasan, A. Islam, O. Miotto, R. Amato, B. MacInnis, J. Stalker, D.P. Kwiatkowski, Z. Bozdech, A. Jeeyapant, P.Y. Cheah, T. Sakulthaew, J. Chalk, B. Intharabut, K. Silamut, S.J. Lee, B. Vihokhern, C. Kunasol, M. Imwong, J. Tarning, W.J. Taylor, S. Yeung, C.J. Woodrow, J.A. Flegg, D. Das, J. Smith, M. Venkatesan, C. V. Plowe, K. Stepniewska, P.J. Guerin, A.M. Dondorp, N.P. Day, N.J. White, Spread of artemisinin resistance in Plasmodium falciparum malaria, N Engl J Med. 371 (2014) 411–423.

[2] Q.Q. Zhang, G.G. Ying, C.G. Pan, Y.S. Liu, J.L. Zhao, Comprehensive evaluation of antibiotics emission and fate in the river basins of China: Source analysis, multimedia modeling, and linkage to bacterial resistance, Environ Sci Technol. 49 (2015) 6772–6782.

[3] S.J. Sucheck, A.L. Wong, K.M. Koeller, D.D. Boehr, K.A. Draker, P. Sears, G.D. Wright, C.H. Wong, Design of bifunctional antibiotics that target bacterial rRNA and inhibit resistance-causing enzymes [11], J Am Chem Soc. 122 (2000) 5230–5231.

[4] M. Rbaa, A. Oubihi, H. Hajji, B. Tüzün, A. Hichar, E.H. Anouar, E. Berdimurodov, M.A. Ajana, A. Zarrouk, B. Lakhrissi, Synthesis, bioinformatics and biological evaluation of novel pyridine based on 8-hydroxyquinoline derivatives as antibacterial agents: DFT, molecular docking and ADME/T studies, J Mol Struct. 1244 (2021) 130934.

[5] Y. Bouzian, Y. Sert, K. Khalid, L. Van Meervelt, K. Chkirate, L. Mahi, N.H. Ahabchane, A. Talbaoui, E.M. Essassi, Synthesis, spectroscopic characterization, DFT, molecular docking and in vitro antibacterial potential of novel quinoline derivatives, J Mol Struct. 1246 (2021) 131217.

[6] R. Kaur, K. Kumar, Synthetic and medicinal perspective of quinolines as antiviral agents, Eur J Med Chem. 215 (2021) 113220.

[7] H.R. Bhat, S.K. Gupta, U.P. Singh, Discovery of potent, novel antibacterial hybrid conjugates from 4-aminoquinoline and 1,3,5-triazine : design, synthesis and antibacterial evaluation, RSC Adv. 2 (2012) 12690–12695.

[8] P.P. Thakare, A.D. Shinde, A.P. Chavan, N. V. Nyayanit, V.D. Bobade, P.C. Mhaske, Synthesis and Biological Evaluation of New 1,2,3-Triazolyl-Pyrazolyl-Quinoline Derivatives as Potential Antimicrobial Agents, ChemistrySelect. 5 (2020) 4722–4727.

[9] G.Z. Yang, J.K. Zhu, X.D. Yin, Y.F. Yan, Y.L. Wang, X.F. Shang, Y.Q. Liu, Z.M. Zhao, J.W. Peng, H. Liu, Design, Synthesis, and Antifungal Evaluation of Novel Quinoline Derivatives Inspired from Natural Quinine Alkaloids, J Agric Food Chem. 67 (2019) 11340–11353.

[10] K. Douadi, S. Chafaa, T. Douadi, M. Al-Noaimi, I. Kaabi, Azoimine quinoline derivatives: Synthesis, classical and electrochemical evaluation of antioxidant, anti-inflammatory, antimicrobial activities and the DNA / BSA binding, J Mol Struct. 1217 (2020) 128305.

[11] H. Kumar, V. Devaraji, R. Joshi, M. Jadhao, P. Ahirkar, R. Prasath, P. Bhavana, S.K. Ghosh, Antihypertensive activity of a quinoline appended chalcone derivative and its site-specific binding interaction with a relevant target carrier protein, RSC Adv. 5 (2015) 65496–65513.

[12] A. Singh, M. Kalamuddin, M. Maqbool, A. Mohmmed, P. Malhotra, N. Hoda, Quinoline carboxamide core moiety-based compounds inhibit P. falciparum falcipain-2: Design, synthesis and antimalarial efficacy studies, Bioorg Chem. 108 (2021) 104514.

[13] B. Sureshkumar, Y.S. Mary, C.Y. Panicker, S. Suma, S. Armaković, S.J. Armaković, C. Van Alsenoy, B. Narayana, Quinoline derivatives as possible lead compounds for anti-malarial drugs: Spectroscopic, DFT and MD study, Arabian Journal of Chemistry. 13 (2020) 632–648.

[14] M. Sankaran, C. Kumarasamy, U. Chokkalingam, P.S. Mohan, Synthesis, antioxidant and toxicological study of novel pyrimido quinoline derivatives from 4-hydroxy-3-acyl quinolin-2-one, Bioorg Med Chem Lett. 20 (2010) 7147–7151.

[15] P. Panda, S. Chakroborty, Navigating the Synthesis of Quinoline Hybrid Molecules as Promising Anticancer Agents, ChemistrySelect. 5 (2020) 10187–10199.

[16] P. Kala, S. Khasim Sharif, C. Murali Krishna, D. Ramachandran, Design, synthesis, and anticancer evaluation of 1,2,4-oxadiazole functionalized quinoline derivatives, Medicinal Chemistry Research. 29 (2020) 136–144.

[17] Z. Xu, C. Gao, Q.C. Ren, X.F. Song, L.S. Feng, Z.S. Lv, Recent advances of pyrazole-containing derivatives as anti-tubercular agents, Eur J Med Chem. 139 (2017) 429–440.

[18] A.R. Chabukswar, B.S. Kuchekar, S.C. Jagdale, P.D. Lokhande, V. V. Chabukswar, S.U. Shisodia, R.H. Mahabal, A.M. Londhe, N.S. Ojha, Synthesis and evaluation of analgesic, anti-asthmatic activity of (E)-1-(8-hydroxyquinolin-7-yl)-3-phenylprop-2-en-1 ones, Arabian Journal of Chemistry. 9 (2016) 704–712.

[19] J. Mo, H. Yang, T. Chen, Q. Li, H. Lin, F. Feng, W. Liu, W. Qu, Q. Guo, H. Chi, Y. Chen, H. Sun, Design, synthesis, biological evaluation, and molecular modeling studies of quinoline-ferulic acid hybrids as cholinesterase inhibitors, Bioorg Chem. 93 (2019) 103310.

[20] R.D. Overacker, S. Banerjee, G.F. Neuhaus, S. Milicevic Sephton, A. Herrmann, J.A. Strother, R. Brack-Werner, P.R. Blakemore, S. Loesgen, Biological evaluation of molecules of the azaBINOL class as antiviral agents: Inhibition of HIV-1 RNase H activity by 7-isopropoxy-8-(naphth-1-yl)quinoline, Bioorg Med Chem. 27 (2019) 3595–3604.

[21] K.N. Kreuzer, N.R. Cozzarelli, Escherichia coli mutants thermosensitive for deoxyribonucleic acid gyrase subunit A: Effects on deoxyribonucleic acid replication, transcription, and bacteriophage growth, J Bacteriol. 140 (1979) 424–435.

[22] E. Orr, W.L. Staudenbauer, An Escherichia coli mutant thermosensitive in the B subunit of DNA gyrase: Effect on the structure and replication of the colicin E1 plasmid in vitro, MGG Molecular & General Genetics. 181 (1981) 52–56.

[23] P. Shrivas, N. Punyapreddiwar, A. Wankhade, S. Zodape, U. Pratap, Baker's yeast catalyzed Henry reaction: Biocatalytic C-C bond formation, Iranian Journal of Catalysis. 7 (2017) 337–340.

[24] M.F. Akhlaghi, M. Daeihamed, S.A. Ayatollahi, F. Kobarfard, A. Ata, Design, Synthesis and Evaluation of Substituted Aryl-2-Nitrovinyl Derivatives as Small Molecules Proteasome Inhibitors, Iran J Pharm Res. 17 (2018) 906.

[25] H. Louis, Seances CRH, Académie Des Sciences. 120 (1895) 1265–1267.

[26] A. Das, R.I. Kureshy, K.J. Prathap, M.K. Choudhary, G.V.S. Rao, N.U.H. Khan, S.H.R. Abdi, H.C. Bajaj, Chiral recyclable Cu(II)-catalysts in nitroaldol reaction of aldehydes with various nitroalkanes and its application in the synthesis of a valuable drug (R)-isoproterenol, Appl Catal A Gen. 459 (2013) 97–105.

[27] R.I. Kureshy, A. Das, N.U.H. Khan, S.H.R. Abdi, H.C. Bajaj, Cu(II)-macrocylic [H4]salen catalyzed asymmetric nitroaldol reaction and its application in the synthesis of α1-adrenergic receptor agonist (R)-phenylephrine, ACS Catal. 1 (2011) 1529–1535.

[28] A. Roy, L.A. Reddy, N. Dwivedi, J. Naram, R. Swapna, G.C. Malakondaiah, M. Ravikumar, D. Bhalerao, T.B. Pratap, P.P. Reddy, A. Bhattacharya, R. Bandichhor, Diastereoselective synthesis of a core fragment of ritonavir and lopinavir, Tetrahedron Lett. 52 (2011) 6968–6970.

[29] R.W. Fitch, G.D. Sturgeon, S.R. Patel, T.F. Spande, H.M. Garraffo, J.W. Daly, R.H. Blaauw, Epiquinamide: A Poison That Wasn't from a Frog That Was, J Nat Prod. 72 (2009) 243–247.

[30] N. Mujafarkani, D.C. Agurokpon, R.A. Hussien, O. V. Ayoola, I.F. Alshdoukhi, G. Sampathkumar, A.A. Alodhayb, S.E. Ogbodo, I. Benjamin, A.J. Ahamed, R.O. Ogar, H. Louis, Antimicrobial activity of guanidine-based terpolymers: Synthesis, Spectroscopy (FT-IR, 1H, and 13C NMR), Quantum chemical investigation, and molecular docking, J Mol Struct. 1298 (2024) 137005.

[31] T. Zandvakili, S. Jamil Fatemi, S. Yousef Ebrahimipour, H. Ebrahimnejad, J. Castro, M. Dusek, V. Eigner, Deferasirox pyridine solvate and its Cu(II) complex: Synthesis, crystal structure, Hirshfeld surface analysis, antimicrobial assays and antioxidant activity, J Mol Struct. 1249 (2022) 131525.

[32] M. Salihović, M. Pazalja, S. Špirtović Halilović, E. Veljović, I. Mahmutović-Dizdarević, S. Roca, I. Novaković, S. Trifunović, Synthesis, characterization, antimicrobial activity and DFT study of some novel Schiff bases, J Mol Struct. 1241 (2021) 130670.

[33] O. Khaoua, N. Benbellat, S. Zeroual, S. Mouffouk, S. Golhen, A. Gouasmia, H. Chermette, H. Haba, Combined experimental, computational studies (synthesis, crystal structural, DFT calculations, spectral analysis) and biological evaluation of the new homonuclear complex Di-μ-benzoato-bis [benzoatodipyridine-cobalt (II)], J Mol Struct. 1273 (2023) 134331.

[34] A. D. Becke, Density-functional thermochemistry. III. The role of exact exchange, J Chem Phys. 98 (1993) 5648–5652.

[35] C. Lee, W. Yang, R.G. Parr, Development of the Colle-Salvetti correlation-energy formula into a functional of the electron density, Physical Review B Condens Matter. 37 (1988) 785–789.

[36] E. J. Baerends, T. Ziegler, A. J. Atkins, J. Autschbach, D. Bashford, A. Bérces, F. M. Bickelhaupt, C. Bo, P. M. Boerrigter, L. Cavallo, D. P. Chong, D. V. Chulhai, L. Deng, R. M. Dickson, J. M. Dieterich, D. E. Ellis, M. van Faassen, L. Fan, T. H. Fischer, C. Fonseca Guerra, M. Franchini, A. Ghysels, A. Giammona, S. J. A. van Gisbergen, A. W. Götz, J. A. Groeneveld, O. V. Gritsenko, M. Grüning, S. Gusarov, F. E. Harris, P. van den Hoek, C. R. Jacob, H. Jacobsen, L. Jensen, J. W. Kaminski, G. van Kessel, F. Kootstra, A. Kovalenko, M. V. Krykunov, E. van Lenthe, D. A. McCormack, A. Michalak, M. Mitoraj, S. M. Morton, J. Neugebauer, V. P. Nicu, L. Noodleman, V. P. Osinga, S. Patchkovskii, M. Pavanello, C. A. Peeples, P. H. T. Philipsen, D. Post, C. C. Pye, W. Ravenek, J. I. Rodriguez, P. Ros, R. Rüger, P. R. T. Schipper, H. van Schoot, G. Schreckenbach, J. S. Seldenthuis, M. Seth, J. G. Snijders, M. Solà, M. Swart, D. Swerhone, G. te Velde, P. Vernooijs, L. Versluis, L. Visscher, O. Visser, F. Wang, T. A.Wesolowski, E. M. van Wezenbeek, G. Wiesenekker, S. K. Wolff, T. K. Woo, A. L. Yakovlev, ADF2022.103, SCM, Theoretical Chemistry, Vrije Universiteit, Amsterdam, The Netherlands, http://www.scm.com., (n.d.).

[37] J.P. Perdew, K. Burke, M. Ernzerhof, Generalized Gradient Approximation Made Simple , Phys Rev Lett. 78 (1997) 1396.

[38] A.D. Becke, Density-functional exchange-energy approximation with correct asymptotic behavior, Phys Rev A (Coll Park). 38 (1988) 3098.

[39] C. Lee, W. Yang, R.G. Parr, Development of the Colle-Salvetti correlation-energy formula into a functional of the electron density, Physical Review B. 37 (1988) 785.

[40] A. D. Becke, Density-functional thermochemistry. III. The role of exact exchange, J Chem Phys. 98 (1993) 5648–5652.

[41] C. Adamo, v. Barone, Toward reliable density functional methods without adjustable parameters: The PBE0 model, J Chem Phys. 110 (1999) 6158.

[42] T. Yanai, D. P. Tew, N. C. Handy, A new hybrid exchange–correlation functional using the Coulomb-attenuating method (CAM-B3LYP), Chem Phys Lett. 393 (2004) 51–57.

[43] V. Tognetti, L. Joubert, Density functional theory and Bader's atoms-in-molecules theory: towards a vivid dialogue, Physical Chemistry Chemical Physics. 16 (2014) 14539–14550.

[44] R. F. W. Bader, H. Essén, The characterization of atomic interactions, J Chem Phys. 80 (1983) 1943–1960.

[45] P. Politzer, P.R. Laurence, K. Jayasuriya, Molecular electrostatic potentials: an effective tool for the elucidation of biochemical phenomena, Environ Health Perspect. 61 (1985) 191–202.

[46] J.S. Murray, P. Politzer, The electrostatic potential: an overview, Wiley Interdiscip Rev Comput Mol Sci. 1 (2011) 153–163.

[47] S. Lakshminarayanan, V. Jeyasingh, K. Murugesan, N. Selvapalam, G. Dass, Molecular electrostatic potential (MEP) surface analysis of chemo sensors: An extra supporting hand for strength, selectivity & non-traditional interactions, J Photochem Photobiol. 6 (2021) 100022.

[48] S.R. Gadre, C.H. Suresh, N. Mohan, Electrostatic Potential Topology for Probing Molecular Structure, Bonding and Reactivity, Molecules 2021, Vol. 26, Page 3289. 26 (2021) 3289.

[49] M.U. OriginLab Corporation: Northampton, OriginLab Corporation. Origin(Pro), Version Number 2022 , (2022).

[50] G.M. Morris, H. Ruth, W. Lindstrom, M.F. Sanner, R.K. Belew, D.S. Goodsell, A.J. Olson, AutoDock4 and AutoDockTools4: Automated docking with selective receptor flexibility, J Comput Chem. 30 (2009) 2785–2791.

[51] N.M. O'Boyle, M. Banck, C.A. James, C. Morley, T. Vandermeersch, G.R. Hutchison, Open Babel: An Open chemical toolbox, J Cheminform. 3 (2011) 1–14.

[52] W.L. Delano, The PyMOL Molecular Graphics System, 10 September 2013. Available Online: Http://Www.Pymol.Org. http://www.pymol.org (2002).

[53] O. Meth-Cohn, S. Rhouati, B. Tarnowski, A. Robinson, A versatile new synthesis of quinolines and related fused pyridines. Part 8. Conversion of anilides into 3-substituted quinolines and into quinoxalines, J Chem Soc Perkin 1. (1981) 1537–1543.

[54] D. Zeleke, R. Eswaramoorthy, Z. Belay, Y. Melaku, Synthesis and Antibacterial, Antioxidant, and Molecular Docking Analysis of Some Novel Quinoline Derivatives, J Chem. 2020 (2020).

[55] Z. Cziáky, F. Kóródi, L. Frank, I. Czink, Synthesis and antimycotic activity of new 2-Chloro-3-(2-nitro)ethyl- and (2-nitro)vinylquinolines, Heterocycl Comm. 2 (1996) 63–70.

[56] B. Ledoussal, J. K. Almstead, C. P. Flaim, Novel fluoroquinolone, structure activity, and design of new potent and safe agents." Program and abstracts of the 39th Interscience Conference on Antimicrobial Agents and Chemotherapy (San Francisco), American Society for Microbiology. (1999).

[57] S.M. Moosavinejad, M. Madhoushi, M. Vakili, D. Rasouli, S.M. Moosavinejad, M. Madhoushi, M. Vakili, D. Rasouli, Evaluation of degradation in chemical compounds of wood in historical buildings using FT-IR and FT-Raman vibrational spectroscopy, Maderas. Ciencia y Tecnología. 21 (2019) 381–392.

[58] L.I.U. Shu-Bin, Conceptual density functional theory and some recent developments, Acta Physico-Chimica Sinica. 25 (3) (2009) 590600.

[59] P. Geerlings, F. de Proft, W. Langenaeker, Conceptual density functional theory, Chem Rev. 103 (2003) 1793–1873.

[60] H. Chermette, Chemical reactivity indexes in density functional theory, J Comput Chem. 20 (1999) 129–154.

[61] J.L. Reed, Electronegativity: Chemical hardness I, Journal of Physical Chemistry A. 101 (1997) 7396–7400.

[62] L.H. Mendoza-Huizar, Chemical reactivity of isoproturon, diuron, linuron, and chlorotoluron herbicides in aqueous phase: A theoretical quantum study employing global and local reactivity descriptors, J Chem. 2015 (2015).

[63] P.K. Chattaraj, U. Sarkar, D.R. Roy, Electrophilicity index, Chem Rev. 106 (2006) 2065–2091.

[64] L.R. Domingo, P. Pérez, The nucleophilicity N index in organic chemistry, Org Biomol Chem. 9 (2011) 7168–7175.

[65] K.S. Pitzer, The Nature of the Chemical Bond and the Structure of Molecules and Crystals: An Introduction to Modern Structural Chemistry., J Am Chem Soc. 82 (2002) 4121–4121.

[66] J.S. Murray, P. Politzer, The electrostatic potential: an overview, Wiley Interdiscip Rev Comput Mol Sci. 1 (2011) 153–163.

[67] S.R. Gadre, C.H. Suresh, N. Mohan, Electrostatic Potential Topology for Probing Molecular Structure, Bonding and Reactivity, Molecules 2021, Vol. 26, Page 3289. 26 (2021) 3289.

[68] S. Lakshminarayanan, V. Jeyasingh, K. Murugesan, N. Selvapalam, G. Dass, Molecular electrostatic potential (MEP) surface analysis of chemo sensors: An extra supporting hand for strength, selectivity & non-traditional interactions, J Photochem Photobiol. 6 (2021) 100022.

[69] R.F.W. Bader, Atoms in molecules-a quantum theory, Oxford University Press, New York, 1990.

[70] I. Rozas, I. Alkorta, J. Elguero, Behavior of ylides containing N, O, and C atoms as hydrogen bond acceptors, J Am Chem Soc. 122 (2000) 11154–11161.

[71] R.G.A. Bone, R.F.W. Bader, Identifying and analyzing intermolecular bonding interactions in van der Waals molecules, Journal of Physical Chemistry. 100 (1996) 10892–10911.

[72] E. Orr, W.L. Staudenbauer, An Escherichia coli mutant thermosensitive in the B subunit of DNA gyrase: Effect on the structure and replication of the colicin E1 plasmid in vitro, MGG Molecular & General Genetics. 181 (1981) 52–56.

[73] K.N. Kreuzer, N.R. Cozzarelli, Escherichia coli Mutants Thermosensitive for Deoxyribonucleic Acid Gyrase Subunit A: Effects on Deoxyribonucleic Acid Replication, Transcription, and Bacteriophage Growth, J Bacteriol. 140 (1979) 424–435.

[74] C.A. Lipinski, F. Lombardo, B.W. Dominy, P.J. Feeney, Experimental and computational approaches to estimate solubility and permeability in drug discovery and development settings, Adv Drug Deliv Rev. 46 (2001) 3–26.

[75] A. Daina, O. Michielin, V. Zoete, SwissADME: a free web tool to evaluate pharmacokinetics, drug-likeness and medicinal chemistry friendliness of small molecules, Scientific Reports 2017 7:1. 7 (2017) 1–13.

[76] D.F. Veber, S.R. Johnson, H.Y. Cheng, B.R. Smith, K.W. Ward, K.D. Kopple, Molecular properties that influence the oral bioavailability of drug candidates, J Med Chem. 45 (2002) 2615–2623.

[77] A.K. Ghose, V.N. Viswanadhan, J.J. Wendoloski, A knowledge-based approach in designing combinatorial or medicinal chemistry libraries for drug discovery. 1. A qualitative and quantitative characterization of known drug databases, J Comb Chem. 1 (1999) 55–68.

[78] W.J. Egan, K.M. Merz, J.J. Baldwin, Prediction of drug absorption using multivariate statistics, J Med Chem. 43 (2000) 3867–3877.

[79] Ingo Muegge, Pharmacophore Features of Potential Drugs, Chemistry - A European Journal. 8 (2002) 1976–81.

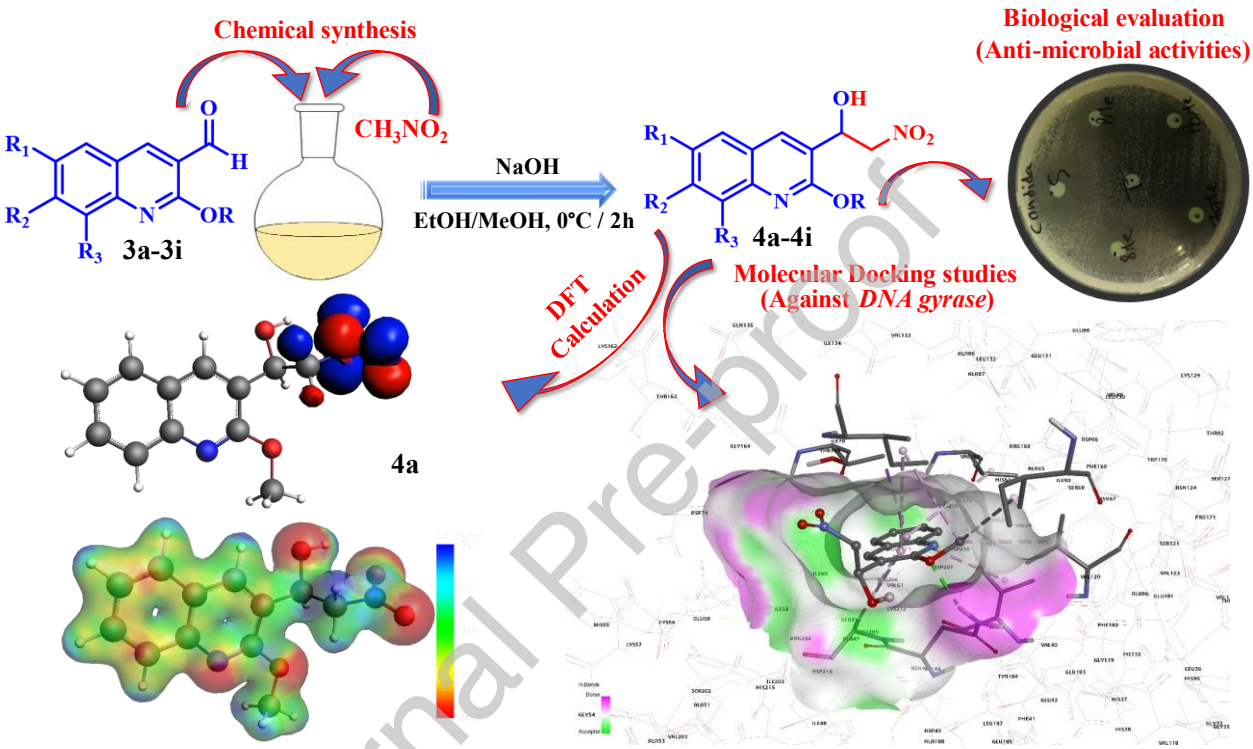

Graphical abstract

Declaration of interests

☒ The authors declare that they have no known competing financial interests or personal relationships that could have appeared to influence the work reported in this paper.

☐ The authors declare the following financial interests/personal relationships which may be considered as potential competing interests: